The discontinuity-enriched finite element method for multiple intersecting discontinuities

Liu, Dongyu; Zhang, Jian; Aragón, Alejandro M.; Simone, Angelo

DOI
10.1016/j.cma.2024.117432

Publication date
2025

Document Version
Final published version

Published in
Computer Methods in Applied Mechanics and Engineering

Computer Methods in Applied Mechanics and Engineering 433 (2025) 117432

Contents lists available at ScienceDirect

Comput. Methods Appl. Mech. Engrg.

journal homepage: www.elsevier.com/locate/cma

The discontinuity-enriched finite element method for multiple intersecting discontinuities

Dongyu Liu [a], Jian Zhang [b], Alejandro M. Aragón [b], Angelo Simone [c,*]

[a] Faculty of Civil Engineering and Geosciences, Delft University of Technology, Stevinweg 1, 2628 CN Delft, The Netherlands
[b] Faculty of Mechanical Engineering, Delft University of Technology, Mekelweg 2, 2628 CD Delft, The Netherlands
[c] Department of Industrial Engineering, University of Padova, Padua, Italy

GRAPHICAL ABSTRACT

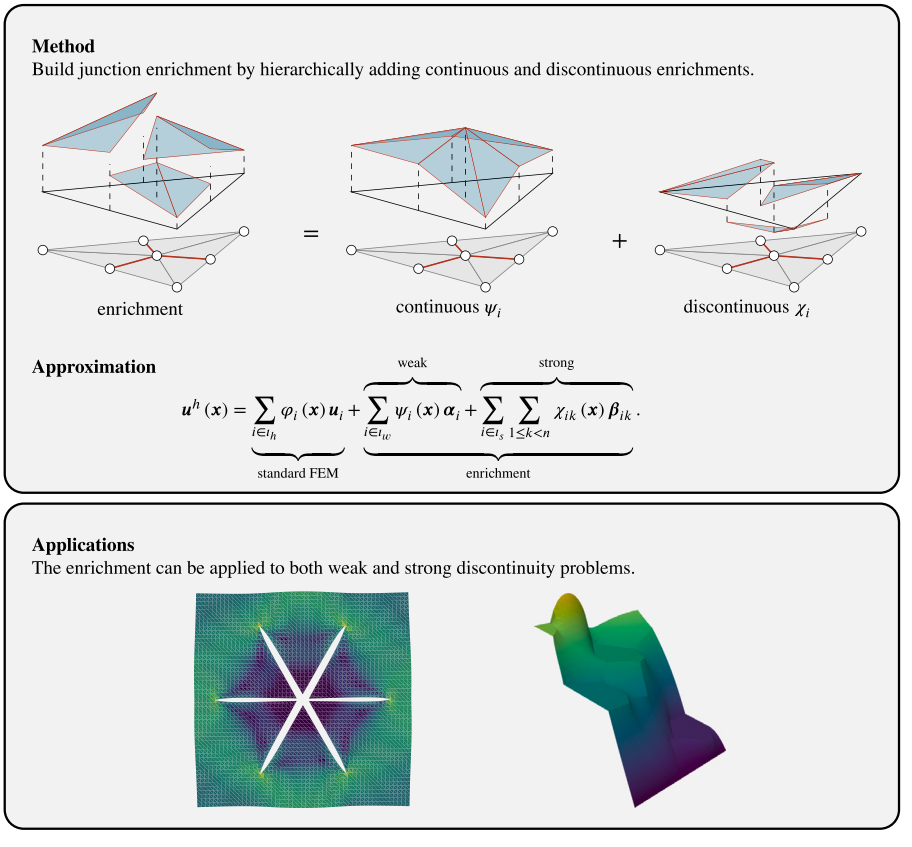

* Corresponding author.
E-mail address: angelo.simone@unipd.it (A. Simone).

https://doi.org/10.1016/j.cma.2024.117432
Received 7 May 2024; Received in revised form 12 September 2024; Accepted 27 September 2024

ARTICLE INFO

Keywords:
Enriched finite element analysis
Discontinuity-Enriched Finite Element Method (DE-FEM)
Intersecting discontinuities
Weak and strong enrichments
Branched cracks
Polycristalline materials

ABSTRACT

We extend the Discontinuity-Enriched Finite Element Method (DE-FEM) to simulate intersecting discontinuities, such as those encountered in polycrystalline materials, multi-material wedge problems, and branched cracks. The proposed hierarchical enrichment functions capture weak and strong discontinuities at junctions within a single formulation. Several numerical applications to branched cracks and polycrystalline microstructures under both thermal and mechanical loads are presented to demonstrate the proposed method. Results indicate that DE-FEM can accurately capture complex discontinuous primal and gradient fields and attain convergence rates comparable to those of standard FEM using fitted meshes. The main advantages of DE-FEM equipped with the proposed junction enrichment functions lie in the method's ability to model intersecting discontinuities using meshes that are completely decoupled from them and its robustness in reproducing correct displacement and strain jumps across them, as demonstrated by a patch test. This work thus highlights the potential of DE-FEM for applications to problems characterized by the presence of multiple intersecting discontinuities, posing a valid alternative to traditional FEM and eXtended/Generalized Finite Element (X/GFEM) Methods.

1. Introduction

Modeling problems with intersecting discontinuities, such as material junctions and branched cracks, has been extensively investigated using both the standard Finite Element Method (FEM) [1–5] and, more recently, the eXtended/Generalized Finite Element Method (X/GFEM) [6–8]. While standard FEM requires geometry matching (fitted) meshes to model the discontinuous field stemming from intersecting discontinuities, X/GFEM allows for decoupling the mesh from all discontinuities. Although both methods are effective in reproducing the kinematics of multiple intersecting discontinuities, remeshing in standard FEM and imposing essential boundary conditions in X/GFEM pose challenges [9]. The Discontinuity-Enriched Finite Element Method (DE-FEM) [10] has been introduced as a solution to these challenges, offering advantages over both standard FEM and X/GFEM. In this work, we extend DE-FEM to address problems involving multiple intersecting discontinuities.

This paper deals with the numerical approximation of problems characterized by discontinuous fields, commonly encountered in fractured solids or materials with spatially variable properties such as polycrystalline aggregates. These problems share similar features in the sense that the numerical approximation of those discontinuous fields can be obtained by means of intersecting discontinuities. Mathematically, these problems result in C^0-continuous and/or C^{-1}-continuous fields, referred henceforth as weak and strong discontinuities, respectively. The modeling of such problems has progressed significantly since the use of discrete springs to represent cohesive forces across discontinuities (refer for instance to the work of Yutaka and Che [11]). Recent applications extend to problems involving intersecting discontinuities, such as grain boundary problems [12–14], crack branching [15,16], and fragmentation [17]. Despite approaches that make use of non-body-fitted grids [18,19], in practical applications, standard FEMs remain the de facto choice despite their intricate meshing procedures. Conversely, X/GFEMs have shown promise in academic scenarios, leveraging special enrichment functions to address meshing challenges for both stationary and evolving discontinuities. For instance, Daux et al. [6] used XFEM to model arbitrarily branched cracks, where cross and star shaped cracks were modeled with unfitted meshes by using a junction enrichment that is built upon step functions. The accuracy of the method was demonstrated by comparing the stress intensity factors (SIFs) of a series of tests consisting of different branched crack configurations with reference solutions. The method was later extended by Belytschko et al. [20] to model dynamic crack branching. Simone et al. [7] used GFEM to model strong discontinuities in polycrystalline aggregates, with an accuracy similar to that of standard FEM with fitted meshes; the utilization of a uniform grain enrichment function proved to be significantly simpler when compared to the junction enrichment of Daux et al. [6]. Aragón et al. [8] proposed the use of the distance function as an enrichment to model weakly discontinuous junctions and showed that, while linear approximations require a correction to recover the accuracy lost in blending elements [21], quadratic approximations were optimal without the need for the correction. Nevertheless, X/GFEM approaches come with inherent drawbacks, such as the loss of accuracy in blending elements with non-constant enrichment functions [21], the need for special techniques to enforce non-homogeneous Dirichlet boundary conditions when enrichments do not vanish at Dirichlet boundaries [9,22], and the need for a stable generalized finite element method (SGFEM) to control the condition number of system matrices when discontinuities get arbitrarily close to nodes of the original discretization [23,24]. Although these issues could be circumvented, to date it is not possible to recover smooth tractions in embedded Dirichlet boundaries (reactions), even with the use of stabilization techniques [25].

Another family of discontinuity-enriched methods emerged to address the challenges posed by X/GFEM. The Interface-enriched Generalized Finite Element Method (IGFEM) [26–28], first proposed to solve problems with weak discontinuities, was later generalized to the Discontinuity-Enriched Finite Element Method (DE-FEM) [10,29] to solve problems containing both weak and strong discontinuities. These techniques place enriched nodes directly along discontinuities instead than to nodes of the original mesh as in X/GFEM. There are numerous advantages to this since many properties of standard FEM that are lost in X/GFEM due to the use of enrichments are recovered, including (i) Enrichment functions are local to cut elements by construction so there are no blending element issues; (ii) Enrichments are exactly zero at nodes of the original mesh, and thus standard degrees of freedom

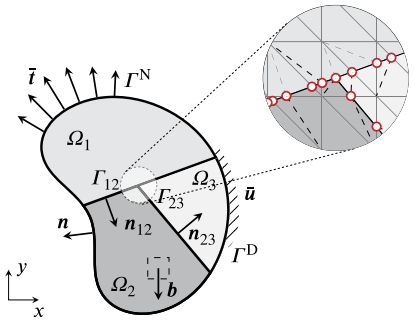

Fig. 1. A two-dimensional domain Ω composed of disjoint subdomains Ω_i such that $\overline{\Omega} = \cup_i \overline{\Omega}_i$ and $\Gamma_{ij} = \overline{\Omega}_i \cap \overline{\Omega}_j \, (i \neq j)$. Dirichlet and Neumann boundary conditions are prescribed on Γ_i^{D} and Γ_i^{N}, respectively. The zoomed-in inset shows the unfitted mesh intersected by discontinuity segments, forming a triple junction. The red circles indicate new nodes with enriched degrees of freedom. The background mesh is depicted with thin solid lines, while the integration elements in the elements cut by the discontinuities are shown with dashed lines.

(DOFs) retain their physical meaning; (iii) Prescribing non-homogeneous essential boundary conditions is as straightforward as in standard FEM, even on immersed boundaries [27]; (iv) Discontinuity-enriched formulations are so far the only enriched FEMs that allow for the transfer of smooth cohesive tractions across internal boundaries [10], smooth tractions for problems that couple non-conforming discretizations and contact [30], and the recovery of smooth reactive tractions from Dirichlet boundaries [27]; and (v) The condition number of stiffness matrices grows at the same rate as in standard FEM, i.e., as $\mathcal{O}(h^{-2})$—this is accomplished either by scaling enrichments as discontinuities approach standard mesh nodes or by using a simple Jacobi-like diagonal preconditioner [28]. Therefore, discontinuity-enriched formulations, while decoupling the mesh from discontinuities, recover many of the properties of standard FEM that are lost in X/GFEM due to the use of enriched spaces. In the context of strong discontinuities, DE-FEM was introduced for 2-D fracture problems [10]. Since then the methodology has been developed for 3-D problems [29], combined with discontinuities described by Non-Uniform Rational B-Splines (NURBS) [31], and developed as an immersed boundary (fictitious domain) technique for modeling embedded discontinuities [27]. Nevertheless, the current DE-FEM formulation lacks the capability to represent the kinematics of intersecting discontinuities. This deficiency is addressed in this work.

In this paper we introduce a junction enrichment for the discontinuity-enriched finite element method, presenting a versatile formulation capable of effectively handling problems featuring multiple intersecting discontinuities. The junction enrichment contains both weak and strong contributions, constructed using a linear combination of Lagrange shape functions in integration subdomains, ensuring vanishing enrichment at the original mesh nodes. A notable feature of the enrichment scheme, as in the original DE-FEM [10] for single discontinuities, is the ability to switch off the strong enrichment contribution. This allows for the recovery of IGFEM [26] approximation spaces and enables the modeling of problems characterized solely by the presence of discontinuous gradient fields. Through numerical examples we demonstrate the robustness and accuracy of our method, achieving similar accuracy to X/GFEM while preserving all the aforementioned advantages of DE-FEM.

2. Problem description and formulation

Consider a domain $\Omega \subset \mathbb{R}^2$ as shown in Fig. 1. The domain is partitioned into distinct, non-overlapping subdomains Ω_i ($i \in \iota_g$, with ι_g the index set for the subdomains) with the domain closure $\overline{\Omega} = \cup_i \overline{\Omega}_i$. The domain is bounded by $\Gamma = \overline{\Omega} \backslash \Omega$ with the outward unit normal vector denoted by $\boldsymbol{n}$. Boundary Γ is decomposed into disjoint parts Γ_i^{D} and Γ_i^{N} where essential (Dirichlet) and natural (Neumann) boundary conditions are prescribed, respectively. The intersection $\Gamma_{ij} = \overline{\Omega}_i \cap \overline{\Omega}_j$ ($i \neq j$) represents either a weak or strong discontinuity at the interface between subdomains i and j. With reference to subdomain i, vector $\boldsymbol{n}_{ij} (= -\boldsymbol{n}_{ji})$ indicates the outward unit normal vector to boundary Γ_{ij} pointing towards subdomain j.

In this work we examine the application of the method to heat conduction and elastostatics boundary value problems. For heat conduction, we seek to find the primal (temperature) field $u \in \mathcal{U}(\Omega)$ such that

$$a(u, v) = L(v) \qquad \forall v \in \mathcal{V}(\Omega), \tag{1}$$

where bilinear and linear forms are, respectively, given by

$$a(u, v) = \sum_{i \in \iota_g} \int_{\Omega_i} \nabla v_i \cdot \left(\boldsymbol{\kappa}_i \nabla u_i \right) \mathrm{d}\Omega \quad \text{and} \quad L(v) = \sum_{i \in \iota_g} \left[\int_{\Omega_i} v_i f_i \, \mathrm{d}\Omega + \int_{\Gamma_i^{\mathrm{N}}} v_i \bar{q}_i \, \mathrm{d}\Gamma \right]. \tag{2}$$

In (2) we denote by u_i the restriction of the temperature field to the ith subdomain, i.e., $u_i \equiv u|_{\Omega_i}$, and the same holds for other subscripted quantities; we also denote by $\boldsymbol{\kappa}_i$ the conductivity tensor, f_i the heat source, and $\bar{q}_i$ and $\bar{u}_i$ the prescribed heat flux and temperature, respectively. Trial solution and test function are taken, respectively, from the sets

$$\mathcal{U}(\Omega) = \left\{ u \in L^2(\Omega), \, u_i \in \mathcal{H}^1(\Omega_i), \; u|_{\Gamma_i^{\mathrm{D}}} = \bar{u}_i \right\} \quad \text{and} \quad \mathcal{V}(\Omega) = \left\{ v \in L^2(\Omega), \, v_i \in \mathcal{H}^1(\Omega_i), \; v|_{\Gamma_i^{\mathrm{D}}} = 0 \right\}, \tag{3}$$

where $\mathcal{H}^1(\Omega_i)$ is the first-order Sobolev space. In the heat conduction problem discussed in Section 5.5 we restrict the analysis to weak discontinuities, and therefore no jump of the primal field is included in (2).

For the elastostatics problem, we seek to find the vectorial displacement field $\boldsymbol{u} \in \mathcal{U}(\Omega)$ such that

$$a(\boldsymbol{u}, \boldsymbol{v}) = L(\boldsymbol{v}) \qquad \forall \boldsymbol{v} \in \mathcal{V}(\Omega), \tag{4}$$

where, as in the reference DE-FEM paper [10],

$$a(\boldsymbol{u}, \boldsymbol{v}) = \sum_{i \in \iota_g} \int_{\Omega_i} \boldsymbol{\epsilon}_i(\boldsymbol{v}_i) : \boldsymbol{\sigma}_i(\boldsymbol{u}_i)\, \mathrm{d}\Omega \quad \text{and} \quad L(\boldsymbol{v}) = \sum_{i \in \iota_g} \left[\int_{\Omega_i} \boldsymbol{v}_i \cdot \boldsymbol{b}_i\, \mathrm{d}\Omega + \int_{\Gamma_i^{\mathrm{N}}} \boldsymbol{v}_i \cdot \bar{\boldsymbol{t}}_i\, \mathrm{d}\Gamma \right] + \sum_{i \neq j} \int_{\Gamma_{ij}} [\![\boldsymbol{v}_i]\!] \cdot \boldsymbol{t}_{ij}^c\, \mathrm{d}\Gamma, \tag{5}$$

with $\boldsymbol{\epsilon}_i(\boldsymbol{u}_i) = \frac{1}{2}\left(\boldsymbol{\nabla}\boldsymbol{u}_i + \boldsymbol{\nabla}\boldsymbol{u}_i^{\mathsf{T}}\right)$ the linearized strain tensor, $\boldsymbol{\sigma}_i$ the Cauchy stress tensor, $\boldsymbol{b}_i$ the body force vector, $\boldsymbol{t}_{ij}^c$ the vector of cohesive tractions across a discontinuity Γ_{ij}, and $\bar{\boldsymbol{u}}_i$ and $\bar{\boldsymbol{t}}_i$ prescribed displacements and tractions, respectively. Stress and strain tensors are related through Hooke's law by $\boldsymbol{\sigma}_i = \boldsymbol{C}_i : \boldsymbol{\epsilon}_i$, where $\boldsymbol{C}_i$ is the fourth-order linear elasticity tensor. The symbol $[\![\cdot]\!]$ denotes the jump operator across a discontinuity. The vector-valued trial solution $\boldsymbol{u}$ and test function $\boldsymbol{v}$ are taken, respectively, from

$$\mathcal{U}(\Omega) = \left\{ \boldsymbol{u} \in \left[L^2(\Omega)\right]^2,\ \boldsymbol{u}_i \in \left[\mathcal{H}^1(\Omega_i)\right]^2,\ \boldsymbol{u}|_{\Gamma_i^{\mathrm{D}}} = \bar{\boldsymbol{u}}_i \right\} \quad \text{and} \quad \mathcal{V}(\Omega) = \left\{ \boldsymbol{v} \in \left[L^2(\Omega)\right]^2,\ \boldsymbol{v}_i \in \left[\mathcal{H}^1(\Omega_i)\right]^2,\ \boldsymbol{v}|_{\Gamma_i^{\mathrm{D}}} = \boldsymbol{0} \right\}. \tag{6}$$

Eq. (5) is used to model problems with cohesive strong discontinuities (a C^{-1}-continuous field) in Sections 5.1 and 5.4. The last term is, however, neglected in problems with only weak discontinuities (Section 5.2) or traction-free strong discontinuities (Sections 5.3.1 and 5.3.2).

To solve the finite dimensional forms of (1) and (4), the domain is discretized into E finite elements so that the discretized domain $\Omega^h = \mathrm{int}\left(\cup_{i=1}^{E} \bar{e}_i\right) \approx \Omega$ such that $e_i \cap e_j = \varnothing\ \forall i \neq j$. We follow a Galerkin procedure, whereby trial and weight functions are chosen from a discontinuity-enriched finite element space that incorporates the kinematics of discontinuities in the primal field and its gradient. This space, which is endowed with characteristic features of the discontinuous field, is defined for elastostatics by extending the definition in [10], resulting in

$$\mathcal{S}_e^h(\Omega^h) = \left\{ \boldsymbol{u}^h(\boldsymbol{x}) \,\middle|\, \boldsymbol{u}^h(\boldsymbol{x}) = \underbrace{\sum_{i \in \iota_h} \varphi_i(\boldsymbol{x})\, \boldsymbol{u}_i}_{\text{standard}} + \underbrace{\overbrace{\sum_{i \in \iota_w} \psi_i(\boldsymbol{x})\, \boldsymbol{\alpha}_i}^{\text{weak}} + \overbrace{\sum_{i \in \iota_s} \sum_{1 \leq k < n} \chi_{ik}(\boldsymbol{x})\, \boldsymbol{\beta}_{ik}}^{\text{strong}}}_{\text{enrichment}},\quad \boldsymbol{u}_i, \boldsymbol{\alpha}_i, \boldsymbol{\beta}_{ik} \in \mathbb{R}^2 \right\} \subset \mathcal{U}(\Omega), \tag{7}$$

where indices ι_h, ι_w, and ι_s represent index sets of standard, weak, and strong nodes, respectively. In (7) the standard finite element component is spanned by linear Lagrange shape functions φ_i associated to standard DOFs $\boldsymbol{u}_i$. This space is augmented by enrichment terms that incorporate information about the discontinuities. In the latter, the behavior at weak discontinuities is captured by weak enrichment functions ψ_i associated with weak enrichment DOFs $\boldsymbol{\alpha}_i$. When dealing with strong discontinuities, in addition to the weak term that captures the jump in the primal field gradient, the jump in displacement is captured by means of strong enrichment functions χ_{ik} associated with strong enrichment DOFs $\boldsymbol{\beta}_{ik}$. Noteworthy, as discussed in Appendix A, the DE-FEM approximation of an n-fold junction necessitates $n-1$ strong enrichments: a triple junction ($n = 3$) therefore requires one weak enrichment and two strong enrichments ($k = \{1, 2\}$)—we recall that an n-fold junction is defined as the point where n discontinuities meet. Therefore, two discontinuities crossing at a point define a 4-fold junction, also known in the literature as a quadruple point. The expression in (7) is general since in fully split elements that do not contain a junction the standard DE-FEM approximation is recovered (i.e., $n = 2$ and thus $k = \{1\}$). We note in passing that (7) is no different from the approximation proposed by Aragón and Simone [10]. This formulation is indeed also applicable to our model problem, provided adequate enrichment functions for resolving multiple intersecting discontinuities are defined.

It is worth noting that, in the absence of strong discontinuities, the third term in (7) drops out and thus we recover the Interface-enriched Generalized Finite Element Method (IGFEM) [26]. IGFEM was in fact proposed to model problems with discontinuous gradient fields alone, and DE-FEM was build to inherit the approximation properties of IGFEM. DE-FEM can therefore seamlessly model both weak and strong discontinuities within a unified formulation. Consequently, IGFEM spaces are recovered in problems where strong discontinuities are absent. IGFEM spaces are used in the convergence test discussed in Section 5.2 and the solution of the heat conduction example in Section 5.5.

For the heat conduction problem, the eth finite element local conductance matrix and local thermal load vector are given, respectively, by

$$\boldsymbol{k}_e = \int_e \boldsymbol{\nabla}_{\boldsymbol{x}} \boldsymbol{\varphi}^{\mathsf{T}} \boldsymbol{\kappa} \boldsymbol{\nabla}_{\boldsymbol{x}} \boldsymbol{\varphi}\, \mathrm{d}e = \int_{\square} \boldsymbol{\nabla}_{\boldsymbol{x}} \boldsymbol{\varphi}^{\mathsf{T}} \boldsymbol{\kappa} \boldsymbol{\nabla}_{\boldsymbol{x}} \boldsymbol{\varphi} j\, \mathrm{d}\square, \tag{8}$$

and

$$\boldsymbol{f}_e = \int_e \boldsymbol{\varphi}^{\mathsf{T}} f\, \mathrm{d}e + \int_{\partial e \cap \Gamma^{\mathrm{N}}} \boldsymbol{\varphi}^{\mathsf{T}} \bar{q}\, \mathrm{d}\partial e = \int_{\square} \boldsymbol{\varphi}^{\mathsf{T}} f j\, \mathrm{d}\square + \int_{\partial e \cap \Gamma^{\mathrm{N}}} \boldsymbol{\varphi}^{\mathsf{T}} \bar{q} j\, \mathrm{d}\partial\square, \tag{9}$$

where numerical quadrature is conducted on the master element $\square = \{(\xi, \eta) |\ \xi \geq 0, \eta \geq 0, \xi + \eta \leq 1\}$ (with Jacobian j), and $\boldsymbol{\varphi}$ is the shape function vector. Similarly, for elastostatics the stiffness matrix and force vector are computed, respectively, as

$$\boldsymbol{k}_e = \int_e \boldsymbol{B}^{\mathsf{T}} \boldsymbol{C} \boldsymbol{B}\, \mathrm{d}e + \int_{\partial e \cap \Gamma_{ij}} \boldsymbol{M}^{\mathsf{T}} \frac{\partial \boldsymbol{t}_{ij}^c}{\partial [\![\boldsymbol{u}]\!]} \boldsymbol{M}\, \mathrm{d}\partial e = \int_{\square} \boldsymbol{B}^{\mathsf{T}} \boldsymbol{C} \boldsymbol{B} j\, \mathrm{d}\square + \int_{\partial\square \cap \Gamma_{ij}} \boldsymbol{M}^{\mathsf{T}} \frac{\partial \boldsymbol{t}_{ij}^c}{\partial [\![\boldsymbol{u}]\!]} \boldsymbol{M} j\, \mathrm{d}\partial\square, \tag{10}$$

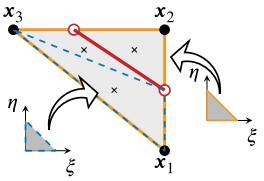

Fig. 2. A mesh element (in orange) cut by a discontinuity (in red). Three integration elements are created, one of which is shown in blue (dashed line). Quadrature points (×) are displayed. Integration over the integration elements involves not only their own mapping but also that of the parent element (in orange). (For interpretation of the references to color in this figure legend, the reader is referred to the web version of this article.)

and

$$\boldsymbol{f}_e = \int_e \boldsymbol{\Phi}^\top \boldsymbol{b}\ \mathrm{d}e + \int_{\partial e \cap \Gamma^\mathrm{N}} \boldsymbol{\Phi}^\top \bar{\boldsymbol{t}}\ \mathrm{d}\partial e + \int_{\partial e \cap \Gamma_{ij}} \boldsymbol{M}^\top \boldsymbol{t}^c_{ij}\ \mathrm{d}\partial e = \int_{\triangle} \boldsymbol{\Phi}^\top \boldsymbol{b} j\ \mathrm{d}\triangle + \int_{\partial\triangle \cap \Gamma^\mathrm{N}} \boldsymbol{\Phi}^\top \bar{\boldsymbol{t}} j\ \mathrm{d}\partial e + \int_{\partial e \cap \Gamma_{ij}} \boldsymbol{M}^\top \boldsymbol{t}^c_{ij} j\ \mathrm{d}\partial\triangle \tag{11}$$

In (10), $\boldsymbol{B}$ is the strain–displacement matrix and $\boldsymbol{C}$ the constitutive matrix, and in (11) $\boldsymbol{\Phi} = \boldsymbol{\varphi} \odot \boldsymbol{I}$ is the shape function matrix—here it is expanded for 2 degrees of freedom per node by means of the Kronecker product $\odot$ with the 2×2 identity matrix $\boldsymbol{I}$). In Eq. (10) and Eq. (11) the terms involving $\boldsymbol{M} = \left[\frac{1-\xi}{2} \quad \frac{1+\xi}{2}\right] \odot \boldsymbol{I}$ essentially perform a 1-D integration along the crack to account for the effect of the cohesive traction [10].

While Eqs. (8)–(11) are computed in a standard manner in elements not crossed by discontinuities, cut elements deserve special attention. One such element is shown schematically in Fig. 2, where a mesh triangular element with coordinates $\{\boldsymbol{x}_i\}_{i=1}^3$ is crossed by a straight discontinuity (in red). Such element is subdivided in so-called *integration elements*, which serve the purpose of integrating smooth functions, since the discontinuity introduces non-smoothness. The quadrature of an integration element follows closely the formulation of Eqs. (8)–(11) with a small modification: The shape function vector is now augmented by weak and strong enrichments as

$$\boldsymbol{\varphi} = \left[\varphi_1 \quad \varphi_2 \quad \varphi_3 \;\middle|\; \psi_1 \quad \cdots \quad \psi_m \;\middle|\; \chi_1 \quad \cdots \quad \chi_n\right], \tag{12}$$

for m weak and n strong enrichments acting in the integration element.

Accordingly, the strain–displacement matrix $\boldsymbol{B}$ is also augmented considering the contributions of enrichment functions, i.e.,

$$\boldsymbol{B} = \left[\begin{array}{cccccc|ccc|ccc|ccc} \frac{\partial\varphi_1}{\partial x} & 0 & \frac{\partial\varphi_2}{\partial x} & 0 & \frac{\partial\varphi_3}{\partial x} & 0 & \frac{\partial\psi_1}{\partial x} & 0 & & \frac{\partial\psi_m}{\partial x} & 0 & \frac{\partial\chi_1}{\partial x} & 0 & & \frac{\partial\chi_n}{\partial x} & 0 \\ 0 & \frac{\partial\varphi_1}{\partial y} & 0 & \frac{\partial\varphi_2}{\partial y} & 0 & \frac{\partial\varphi_3}{\partial y} & 0 & \frac{\partial\psi_1}{\partial y} & \cdots & 0 & \frac{\partial\psi_m}{\partial y} & 0 & \frac{\partial\chi_1}{\partial y} & \cdots & 0 & \frac{\partial\chi_n}{\partial y} \\ \frac{\partial\varphi_1}{\partial y} & \frac{\partial\varphi_1}{\partial x} & \frac{\partial\varphi_2}{\partial y} & \frac{\partial\varphi_2}{\partial x} & \frac{\partial\varphi_3}{\partial y} & \frac{\partial\varphi_3}{\partial x} & \frac{\partial\psi_1}{\partial y} & \frac{\partial\psi_1}{\partial x} & & \frac{\partial\psi_m}{\partial y} & \frac{\partial\psi_m}{\partial x} & \frac{\partial\chi_1}{\partial y} & \frac{\partial\chi_1}{\partial x} & & \frac{\partial\chi_n}{\partial y} & \frac{\partial\chi_n}{\partial x} \end{array}\right]. \tag{13}$$

In addition, it is important to note that two geometry mappings are involved in the numerical quadrature of integration elements: the mapping of the integration element itself (blue mapping) and that of the parent cut element (orange mapping), as shown in Fig. 2. It is worth noting that the same procedure is used when an element contains a junction: The parent cut element is partitioned into integration elements and local arrays are augmented depending on the number of enrichments active on each integration element.

Eqs. (8)–(11) are integrated using numerical Gauss integration with n_GP quadrature points with coordinates $\boldsymbol{\xi}_i$ and weights w_i. Note that a single Gauss point is shown in Fig. 2, which is enough to integrate the arrays exactly. In addition, we note that boundary integrals are implemented as line integrals and are computed only once. This is important because the boundaries of integration elements are often shared by two elements (e.g., when integrating the cohesive traction term). More details on the quadrature of local arrays are given later in Section 4.

The contributions of all local arrays are then assembled in their global counterparts. Denoting by $\mathop{\triangle}$ the standard finite element assembly operator, the global stiffness (or conductance) matrix, and the global force (or thermal load) vector are given by

$$\boldsymbol{K} = \mathop{\triangle}_{e=1}^{E} \boldsymbol{k}_e \quad \text{and} \quad \boldsymbol{F} = \mathop{\triangle}_{e=1}^{E} \boldsymbol{f}_e, \tag{14}$$

respectively. This leads to the discrete linear system of equations $\boldsymbol{K}\boldsymbol{U} = \boldsymbol{F}$. Noteworthy, due to the presence of enrichments, the system can be written as

$$\begin{bmatrix} \boldsymbol{K}_{uu} & \boldsymbol{K}_{u\alpha} & \boldsymbol{K}_{u\beta} \\ \boldsymbol{K}_{u\alpha}^\mathsf{T} & \boldsymbol{K}_{\alpha\alpha} & \boldsymbol{K}_{\alpha\beta} \\ \boldsymbol{K}_{u\beta}^\mathsf{T} & \boldsymbol{K}_{\alpha\beta}^\mathsf{T} & \boldsymbol{K}_{\beta\beta} \end{bmatrix} \begin{bmatrix} \boldsymbol{u} \\ \boldsymbol{\alpha} \\ \boldsymbol{\beta} \end{bmatrix} = \begin{bmatrix} \boldsymbol{f}_u \\ \boldsymbol{f}_\alpha \\ \boldsymbol{f}_\beta \end{bmatrix}, \tag{15}$$

where subscripts u, α, and β make explicit reference to standard, weak enrichment, and strong enrichment contributions, respectively. The expression for the heat conduction problem is a subset of (15) in which strong enrichment terms are neglected.

In DE-FEM, since enrichment functions are nonzero only in cut elements and exactly zero at mesh nodes, non-homogeneous essential boundary conditions can be strongly enforced by directly specifying the values of weak and strong enriched DOFs. Consider in Fig. 3 a mesh element crossed by a discontinuity Γ_{ij}. One of the edges of the element lies along the Dirichlet boundary Γ^D, and

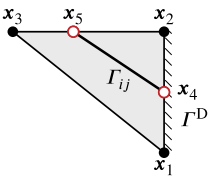

Fig. 3. Finite element crossed by a discontinuity Γ_{ij} and with an edge on the Dirichlet boundary Γ^{D} (hatched region).

thus an essential boundary condition needs to be prescribed at mesh nodes $\boldsymbol{x}_1$ and $\boldsymbol{x}_2$, and at enriched node $\boldsymbol{x}_4$. Since the enrichment functions are exactly zero at mesh nodes $\boldsymbol{x}_1$ and $\boldsymbol{x}_2$, prescribing the primal field at these locations is done as in standard FEM. As for the enriched node $\boldsymbol{x}_4$, when dealing with a weak discontinuity, we need to solve a local problem since the element shape functions φ_1 and φ_2 are nonzero at that location. The local problem simply consists in the evaluation of

$$\boldsymbol{\alpha}_4 = \frac{1}{\psi_4}\left(\bar{\boldsymbol{u}}\left(\boldsymbol{x}_4\right) - \varphi_1\left(\boldsymbol{x}_4\right)\bar{\boldsymbol{u}}\left(\boldsymbol{x}_1\right) - \varphi_2\left(\boldsymbol{x}_4\right)\bar{\boldsymbol{u}}\left(\boldsymbol{x}_2\right)\right). \tag{16}$$

In this equation, obtained from (7), $\bar{\boldsymbol{u}}$ is the prescribed displacement field. The last two terms of the equation then represent the standard finite element contribution that results from the linear interpolation of nodal values within the support of the enriched node. The enriched DOFs $\boldsymbol{\alpha}$ obtained through (16) thus represent the missing continuous contribution that needs to be added to the unfitted finite element approximation as discussed next in Section 3. In contrast, when dealing with a strong discontinuity, the strong DOFs at the Dirichlet boundary represent the displacement jump at that location. After determining the values of these enriched DOFs, they are prescribed in the same manner as in standard FEM. This straightforward manner of prescribing non-homogeneous essential boundary conditions can also be done on immersed boundaries, as discussed in van den Boom et al. [27]. A side benefit of placing enriched nodes along discontinuities is that reactive tractions on immersed Dirichlet boundaries are smooth, whereas in X/GFEM they show oscillations even with the Barbosa–Hughes stabilization [25].

As a final remark, it is important to mention that the issue of stability has not been addressed in this study, and none of the approaches discussed in van den Boom et al. [27], Aragón et al. [28], and Zhang et al. [29] (i.e., scaling of the enrichment functions or using a Jacobi-like preconditioner) have been considered.

For more details on the formulation and implementation aspects of the discontinuity-enriched finite element method, the reader is referred to Aragón and Duarte [32].

2.1. Stress intensity factors

Stress intensity factors are crucial parameters in fracture mechanics since they can accurately quantify the stress field near a crack tip. According to LEFM, SIFs K_{I} and K_{II} for opening mode I and sliding mode II, respectively, are defined as

$$\begin{aligned} K_{\mathrm{I}} &= \lim_{r\to 0}\sqrt{2\pi r}\sigma_{yy} \quad \text{at } \theta = 0, \\ K_{\mathrm{II}} &= \lim_{r\to 0}\sqrt{2\pi r}\sigma_{xy} \quad \text{at } \theta = 0, \end{aligned} \tag{17}$$

where (r,θ) is the polar coordinate from the crack tip, σ_{yy} is the normal stress perpendicular to the crack plane, and σ_{xy} the shear stress in the crack plane.

In this work we compute SIFs as in our first work on DE-FEM [10], whereby we use the integration integral [33]

$$I^{(1,2)} = \int_A \left[\left(-\sigma_{ik}^{(1)}\varepsilon_{ik}^{(2)}\delta_{1j} + \sigma_{ij}^{(1)}\frac{\partial u_i^{(2)}}{\partial x_1} + \sigma_{ij}^{(2)}\frac{\partial u_i^{(1)}}{\partial x_1}\right)\frac{\partial q_1}{\partial x_j}\right]\mathrm{d}A, \tag{18}$$

where all quantities refer to a coordinate system placed at the crack tip that is aligned with the crack plane, quantities superscripted with (1) refer to the actual state in the domain due to applied loads, and quantities superscripted with (2) refer to the auxiliary or reference state, typically corresponding to pure mode I or mode II. The latter are given in Appendix B for completeness. The weight function q_1 has a unit magnitude in finite elements completely enclosed by a circle of radius ρ, which delineates the area of the integral, and ramps linearly to zero at the outer nodes of elements intersected by the circle. Therefore, elements fully contained in the area do not contribute to the interaction integral since $\frac{\partial q_1}{\partial x_j} = 0$.

SIFs are related to the interaction integral through

$$I^{(1,2)} = \frac{2}{E^*}\left(K_{\mathrm{I}}^{(1)}K_{\mathrm{I}}^{(2)} + K_{\mathrm{II}}^{(1)}K_{\mathrm{II}}^{(2)}\right) \quad \text{with} \quad E^* = \begin{cases} E & \text{for plane stress,} \\ \dfrac{E}{1-\nu^2} & \text{for plane strain,} \end{cases} \tag{19}$$

where E denotes Young's modulus and ν Poisson's ratio. We obtain SIFs by setting an auxiliary state and then computing (18). For instance, by setting $K_{\mathrm{I}}^{(2)} = 1$ and $K_{\mathrm{II}}^{(2)} = 0$ we can solve (19) for $K_{\mathrm{I}}^{(1)}$. Similarly, we calculate $K_{\mathrm{II}}^{(1)}$ by setting $K_{\mathrm{I}}^{(2)} = 0, K_{\mathrm{II}}^{(2)} = 1$. More details are provided by Aragón and Simone [10].

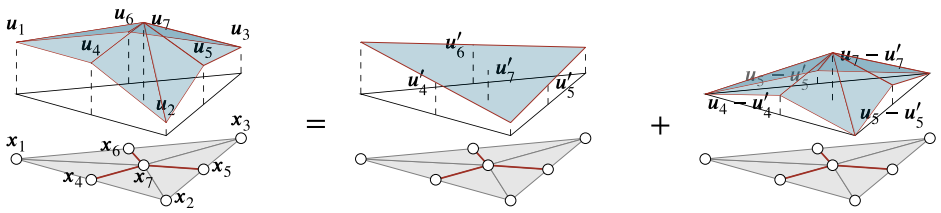

Fig. 4. Two equivalent procedures to construct a C^0-continuous approximation. The standard finite element method is used on the left of the equal sign, whereas a hierarchical procedure is used on the right.

3. DE-FEM formulation for weak and strong intersecting discontinuities

The formulation for a single discontinuity has already been thoroughly discussed by Aragón and Simone [10] and Zhang et al. [29]. In the following we outline the construction of the enrichment strategy for intersecting discontinuities. We start with the weak enrichment, which describes intersecting discontinuities in a C^0-continuous field. We then use this enrichment as a building block for deriving the strong discontinuity enrichment in a C^{-1}-continuous field.

3.1. Weak enrichment

Without loss of generality, we consider three weak discontinuities intersecting within a single triangular domain e partitioned into six linear triangular elements (see Fig. 4). The standard finite element approximation for a vector-valued field is given by

$$\boldsymbol{u}^h(\boldsymbol{x}) = \sum_{i=1}^{7} \varphi_i(\boldsymbol{x})\,\boldsymbol{u}_i, \tag{20}$$

where φ_i is the Lagrange basis associated with standard DOF $\boldsymbol{u}_i$. Because of the nature of the basis functions, (20) is a piece-wise linear interpolation. This field can also be hierarchically constructed by employing an alternative basis, where we expand an existing basis with functions that are designed to reproduce the kinematics of weak discontinuities. Taking Lagrange shape functions $\boldsymbol{\Phi}' = \{\varphi'_i\}_{i=1}^{3}$ such that $\forall \varphi'_i \in \boldsymbol{\Phi}'$, $\operatorname{supp}\varphi'_i = \bigcup_{j=1}^{7} \operatorname{supp}\varphi_j$ and enrichment functions $\psi_i = \varphi_i, i = \{4 \cdots 7\}$ (in essence just a change in notation), the linear field in (20) can be written as

$$\boldsymbol{u}^h(\boldsymbol{x}) = \sum_{i=1}^{3} \varphi'_i(\boldsymbol{x})\,\boldsymbol{u}_i + \sum_{i=4}^{7} \psi_i(\boldsymbol{x})\,\underbrace{\left(\boldsymbol{u}_i - \boldsymbol{u}'_i\right)}_{\boldsymbol{\alpha}_i}, \tag{21}$$

where $\boldsymbol{u}'_j = \sum_{i=1}^{3} \varphi'_i(\boldsymbol{x}_j)\,\boldsymbol{u}_i$, $j = \{4 \cdots 7\}$, i.e., the value of the field at location $\boldsymbol{x}_j$ that is interpolated by the basis $\boldsymbol{\Phi}'$. Noteworthy, the hierarchical representation of the field given by (21) inevitably entails that the partition of unity property of all functions in the triangular domain e no longer holds. However, functions φ'_i still satisfy the Kronecker-δ property among themselves, i.e., $\varphi'_i(\boldsymbol{x}_j) = \delta_{ij}, i, j = \{1 \cdots 3\}$, and similarly for the enrichment functions $\psi_i(\boldsymbol{x}_j) = \delta_{ij}, i, j = \{4 \cdots 7\}$. The two piece-wise linear fields (20) and (21) are equivalent (cf. Fig. 4), i.e.,

$$\sum_{i=1}^{7} \varphi_i(\boldsymbol{x})\,\boldsymbol{u}_i \equiv \sum_{i=1}^{3} \varphi'_i(\boldsymbol{x})\,\boldsymbol{u}_i + \sum_{i=4}^{7} \psi_i(\boldsymbol{x})\,\boldsymbol{\alpha}_i, \tag{22}$$

as long as $\boldsymbol{u}_i = \boldsymbol{u}'_i$, $i = \{1 \cdots 3\}$ and $\boldsymbol{u}_j = \boldsymbol{\alpha}_j + \sum_{i=1}^{3} \varphi'_i(\boldsymbol{x}_j)\,\boldsymbol{u}_i$, $j = \{4 \cdots 7\}$. This can be trivially shown by taking a single element in the patch and verifying that the difference between (20) and (21) is zero. This is tantamount to stating that both sets of basis functions span the same finite element space, i.e., $\operatorname{span}\{\varphi_1 \ldots \varphi_7\} = \operatorname{span}(\varphi'_1 \ldots \varphi'_3, \psi_4 \ldots \psi_7)$.

It is worth noting that the foregoing discussion leaves out of consideration a scaling parameter that is used to scale enrichment functions so as to improve the condition number of stiffness matrices. Notice, however, that scaling enrichment functions does not change the finite element space that is spanned. For more details about how to improve the stability of the enriched formulation, the reader is referred to Aragón et al. [28] and references therein.

3.2. Strong enrichment

We now derive the strong enrichment by considering three strong discontinuities. The resulting C^{-1}-continuous field corresponds to three completely independent kinematic fields. In standard FEM this is accomplished by duplicating nodes across the discontinuity—note that three nodes need to be added to the triple junction. For a fitted mesh (see Fig. 5(a)), there are therefore a total of twelve nodes. The standard finite element interpolation in the triangular domain e is therefore written as

$$\boldsymbol{u}^h(\boldsymbol{x}) = \sum_{i=1}^{12} \varphi_i(\boldsymbol{x})\,\boldsymbol{u}_i, \tag{23}$$

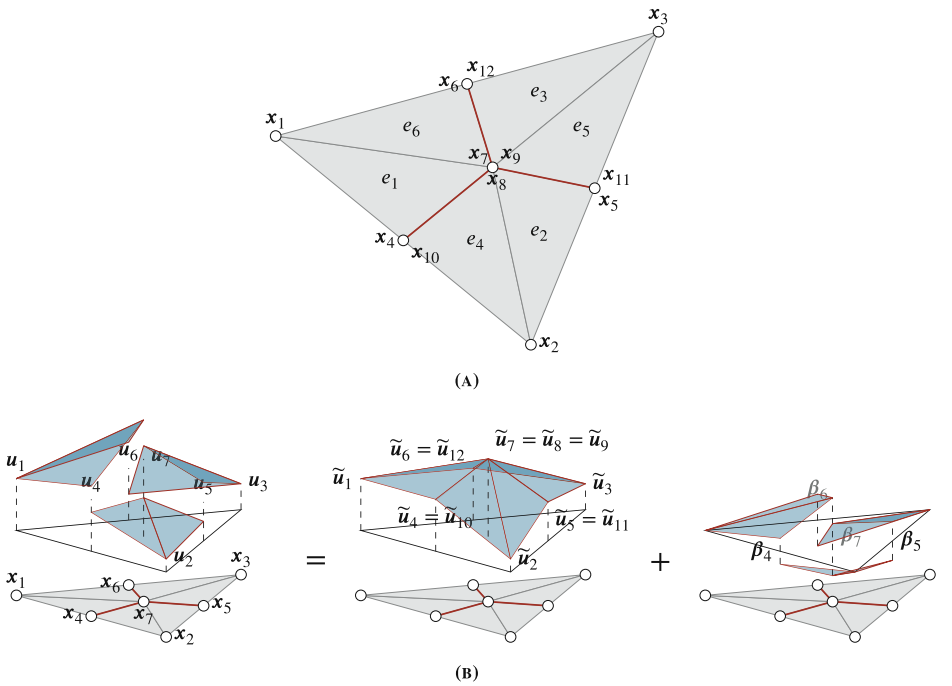

Fig. 5. (A) Triangular domain comprised of six triangular elements. Note that $\boldsymbol{x}_4 = \boldsymbol{x}_{10}$, $\boldsymbol{x}_5 = \boldsymbol{x}_{11}$, $\boldsymbol{x}_6 = \boldsymbol{x}_{12}$, and $\boldsymbol{x}_7 = \boldsymbol{x}_8 = \boldsymbol{x}_9$; (B) Decomposition of the discontinuous field into non-smooth continuous and non-smooth discontinuous components. The non-smooth continuous component, which is also shown on the left of Fig. 4, is given by (21).

which can be recast into

$$\boldsymbol{u}^h(\boldsymbol{x}) = \widetilde{\boldsymbol{u}}^h(\boldsymbol{x}) + \bar{\bar{\boldsymbol{u}}}^h(\boldsymbol{x}), \tag{24}$$

i.e., as the sum of a non-smooth continuous (C^0-continuous) function and a non-smooth discontinuous (C^{-1}-continuous) function as demonstrated next.

Consider, for instance, the lower edge of the triangular domain with nodes $\boldsymbol{x}_1, \boldsymbol{x}_2, \boldsymbol{x}_4$, and $\boldsymbol{x}_{10}$. The field along this edge, due to the fact that other shape functions are zero, can be written as

$$\boldsymbol{u}^h(\boldsymbol{x}) = \varphi_1(\boldsymbol{x})\boldsymbol{u}_1 + \varphi_2(\boldsymbol{x})\boldsymbol{u}_2 + \varphi_4(\boldsymbol{x})\boldsymbol{u}_4 + \varphi_{10}(\boldsymbol{x})\boldsymbol{u}_{10}. \tag{25}$$

The displacement jump along the edge is simply $[\![\boldsymbol{u}^h]\!] = \boldsymbol{u}^h(\boldsymbol{x}_{10}) - \boldsymbol{u}^h(\boldsymbol{x}_4) = \boldsymbol{u}_{10} - \boldsymbol{u}_4 \equiv \boldsymbol{\beta}_4$. We decompose the field along this edge in continuous and discontinuous components as

$$\begin{aligned} \boldsymbol{u}^h(\boldsymbol{x}) = {} & \varphi_1(\boldsymbol{x})\boldsymbol{u}_1 + \varphi_2(\boldsymbol{x})\boldsymbol{u}_2 + \varphi_4(\boldsymbol{x})\left(\boldsymbol{u}_4 + \gamma\boldsymbol{\beta}_4\right) + \varphi_{10}(\boldsymbol{x})\left(\boldsymbol{u}_{10} - (1-\gamma)\boldsymbol{\beta}_4\right) && \text{(continuous)} \\ & - \gamma\varphi_4(\boldsymbol{x})\boldsymbol{\beta}_4 + (1-\gamma)\varphi_{10}(\boldsymbol{x})\boldsymbol{\beta}_4, && \text{(discontinuous)} \end{aligned} \tag{26}$$

where γ is an arbitrary scalar parameter that serves the purpose of splitting the field in continuous and discontinuous parts. Consequently, there is an infinite number of ways to decompose the function in continuous and discontinuous components. Note that $\varphi_4(\boldsymbol{x})\left(\boldsymbol{u}_4 + \gamma\boldsymbol{\beta}_4\right) = \varphi_{10}(\boldsymbol{x})\left(\boldsymbol{u}_{10} - (1-\gamma)\boldsymbol{\beta}_4\right)$ at $\boldsymbol{x}_4 = \boldsymbol{x}_{10}$, and that (26) can be simplified straightforwardly to (25).

This edge analysis can be generalized to describe the field in the entire triangular domain e. Similar to (26), the field is decomposed into continuous and discontinuous components:

$$\boldsymbol{u}^h(\boldsymbol{x}) = \underbrace{\widetilde{\boldsymbol{u}}^h(\boldsymbol{x})}_{\text{continuous}} + \underbrace{\bar{\bar{\boldsymbol{u}}}^h(\boldsymbol{x})}_{\text{discontinuous}}, \tag{27}$$

where

$$\begin{aligned} \widetilde{\boldsymbol{u}}^h(\boldsymbol{x}) = {} & \sum_{i=1}^{3} \varphi_i(\boldsymbol{x})\boldsymbol{u}_i + \varphi_4(\boldsymbol{x})\left(\boldsymbol{u}_4 + \gamma_4\boldsymbol{\beta}_4\right) + \varphi_{10}(\boldsymbol{x})\left(\boldsymbol{u}_{10} - \left(1-\gamma_4\right)\boldsymbol{\beta}_4\right) + \varphi_5(\boldsymbol{x})\left(\boldsymbol{u}_5 + \gamma_5\boldsymbol{\beta}_5\right) \\ & + \varphi_{11}(\boldsymbol{x})\left(\boldsymbol{u}_{11} - \left(1-\gamma_5\right)\boldsymbol{\beta}_5\right) + \varphi_6(\boldsymbol{x})\left(\boldsymbol{u}_6 + \gamma_6\boldsymbol{\beta}_6\right) + \varphi_{12}(\boldsymbol{x})\left(\boldsymbol{u}_{12} - \left(1-\gamma_6\right)\boldsymbol{\beta}_6\right) + \widetilde{\boldsymbol{u}}_j^h, \end{aligned} \tag{28}$$

$$\begin{aligned} \bar{\bar{\boldsymbol{u}}}^h(\boldsymbol{x}) = {} & -\gamma_4\varphi_4(\boldsymbol{x})\boldsymbol{\beta}_4 + \left(1-\gamma_4\right)\varphi_{10}(\boldsymbol{x})\boldsymbol{\beta}_4 - \gamma_5\varphi_5(\boldsymbol{x})\boldsymbol{\beta}_5 + \left(1-\gamma_5\right)\varphi_{11}(\boldsymbol{x})\boldsymbol{\beta}_5 - \gamma_6\varphi_6(\boldsymbol{x})\boldsymbol{\beta}_6 \\ & + \left(1-\gamma_6\right)\varphi_{12}(\boldsymbol{x})\boldsymbol{\beta}_6 + \bar{\bar{\boldsymbol{u}}}_j^h(\boldsymbol{x}), \end{aligned} \tag{29}$$

with $\widetilde{\boldsymbol{u}}_j^h$ and $\bar{\tilde{\boldsymbol{u}}}_j^h$ the continuous and discontinuous field components at the junction, respectively. At the junction there are three overlapping nodes, i.e., $\boldsymbol{x}_7$, $\boldsymbol{x}_8$, and $\boldsymbol{x}_9$ (see Fig. 5). By defining the displacement jump at the junction between nodes $\boldsymbol{x}_7$ and $\boldsymbol{x}_8$ as $\boldsymbol{u}^h\left(\boldsymbol{x}_8\right) - \boldsymbol{u}^h\left(\boldsymbol{x}_7\right) = \boldsymbol{u}_8 - \boldsymbol{u}_7 \equiv \boldsymbol{\beta}_7$, and similarly between nodes $\boldsymbol{x}_8$ and $\boldsymbol{x}_9$ as $\boldsymbol{u}^h\left(\boldsymbol{x}_9\right) - \boldsymbol{u}^h\left(\boldsymbol{x}_8\right) \equiv \boldsymbol{\beta}_8$, the jump between nodes $\boldsymbol{x}_7$ and $\boldsymbol{x}_9$ is simply $\boldsymbol{u}^h\left(\boldsymbol{x}_9\right) - \boldsymbol{u}^h\left(\boldsymbol{x}_7\right) \equiv \boldsymbol{\beta}_7 + \boldsymbol{\beta}_8$—a linear combination of the former two jumps. By using this linear dependency and the continuity constraint of the continuous component (see detailed derivation in Appendix A), we can write the junction components as

$$\widetilde{\boldsymbol{u}}_j^h = (\boldsymbol{u}_7 + \gamma_7\boldsymbol{\beta}_7)(\varphi_7(\boldsymbol{x}) + \varphi_8(\boldsymbol{x}) + \varphi_9(\boldsymbol{x})), \tag{30}$$

$$\bar{\tilde{\boldsymbol{u}}}_j^h = -\gamma_7\varphi_7(\boldsymbol{x})\boldsymbol{\beta}_7 + \left(1-\gamma_7\right)\varphi_8(\boldsymbol{x})\boldsymbol{\beta}_7 + (1-\gamma_7)\varphi_9(\boldsymbol{x})\boldsymbol{\beta}_7 + \varphi_9(\boldsymbol{x})\boldsymbol{\beta}_8. \tag{31}$$

Once again, it can be verified that by replacing (30) and (31), respectively, in (28) and (29), (27) reduces to the standard finite element approximation $\boldsymbol{u}^h(\boldsymbol{x}) = \sum_{i=1}^{12}\varphi_i(\boldsymbol{x})\boldsymbol{u}_i$. Now we simplify the above continuous and discontinuous components at the junction by defining enrichment functions. First, we define the weak enrichment function at the junction as

$$\psi_7(\boldsymbol{x}) = \begin{cases} \varphi_7(\boldsymbol{x}) & \text{for } \boldsymbol{x} \in \left\{e_1, e_6\right\}, \\ \varphi_8(\boldsymbol{x}) & \text{for } \boldsymbol{x} \in \left\{e_2, e_4\right\}, \\ \varphi_9(\boldsymbol{x}) & \text{for } \boldsymbol{x} \in \left\{e_3, e_5\right\}, \end{cases} \tag{32}$$

and the weak enriched DOFs as $\boldsymbol{\alpha}_7 = \boldsymbol{u}_7 - \boldsymbol{u}_7' + \gamma_7\boldsymbol{\beta}_7$. Besides, it is worth noticing that $\boldsymbol{\alpha}_7$ can also be expressed using $\boldsymbol{u}_8$ or $\boldsymbol{u}_9$. These different ways of expressing the weak enriched DOFs are equivalent, as discussed in Appendix A. With the definition of the weak enrichment function, the continuous part at the junction is expressed as

$$\widetilde{\boldsymbol{u}}_j^h = \psi_7(\boldsymbol{x})\boldsymbol{\alpha}_7. \tag{33}$$

Next, with the definitions of the strong enrichments

$$\chi_7(\boldsymbol{x}) = \begin{cases} -\gamma_7\varphi_7(\boldsymbol{x}) & \text{for } \boldsymbol{x} \in \left\{e_1, e_6\right\}, \\ (1-\gamma_7)\varphi_8(\boldsymbol{x}) & \text{for } \boldsymbol{x} \in \left\{e_2, e_4\right\}, \\ (1-\gamma_7)\varphi_9(\boldsymbol{x}) & \text{for } \boldsymbol{x} \in \left\{e_3, e_5\right\}, \end{cases} \quad \text{and} \quad \chi_8(\boldsymbol{x}) = \begin{cases} 0 & \text{for } \boldsymbol{x} \in \left\{e_1, e_6\right\}, \\ 0 & \text{for } \boldsymbol{x} \in \left\{e_2, e_4\right\}, \\ \varphi_9(\boldsymbol{x}) & \text{for } \boldsymbol{x} \in \left\{e_3, e_5\right\}, \end{cases} \tag{34}$$

the field $\bar{\tilde{\boldsymbol{u}}}_j^h(\boldsymbol{x})$ is expressed as

$$\bar{\tilde{\boldsymbol{u}}}_j^h(\boldsymbol{x}) = \chi_7(\boldsymbol{x})\boldsymbol{\beta}_7 + \chi_8(\boldsymbol{x})\boldsymbol{\beta}_8. \tag{35}$$

While in (34) the value of γ_7 is arbitrary, in this work we follow the original approach for computing it based on the relative distance to the intersection location [10].

Finally, similarly to the weak discontinuity case, the approximated field can be expressed as

$$\sum_{i=1}^{12}\varphi_i(\boldsymbol{x})\boldsymbol{u}_i \equiv \underbrace{\sum_{i=1}^{3}\varphi_i'(\boldsymbol{x})\boldsymbol{u}_1}_{\substack{\text{smooth}\\ \text{continuous}}} + \underbrace{\sum_{i=4}^{7}\psi_i(\boldsymbol{x})\boldsymbol{\alpha}_i}_{\substack{\text{non-smooth}\\ \text{continuous}}} + \underbrace{\sum_{i=7,\, i\neq 9}^{12}\chi_i\boldsymbol{\beta}_i}_{\substack{\text{non-smooth}\\ \text{discontinuous}}}, \tag{36}$$

and therefore $\operatorname{span}\left\{\varphi_1 \dots \varphi_{12}\right\} = \operatorname{span}\left(\varphi_1' \dots \varphi_3', \psi_4 \dots \psi_7, \left\{\chi_i\right\}_{i=7,\, i\neq 9}^{12}\right)$, where $\chi_{10}, \chi_{11}, \chi_{12}$ are enrichment functions with displacement jumps at edges, which can be already described by the strong enrichments as defined in the reference DE-FEM paper [10]. The absence of $\boldsymbol{\beta}_9$ in (36) is noteworthy; this omission is a deliberate choice made to avoid linear dependency in the equation, given that $\boldsymbol{\beta}_9 = \boldsymbol{\beta}_7 + \boldsymbol{\beta}_8$. This particular form of (36), without the presence of $\boldsymbol{\beta}_9$, is just one of the possible enrichments that can be derived to eliminate the linear dependency issue. Indeed, we could, for example, have used $\boldsymbol{\beta}_9$ and $\boldsymbol{\beta}_8$ to express $\boldsymbol{\beta}_7$. The three-term expression on the right-hand side of (36), which is comprised of smooth continuous, non-smooth continuous, and non-smooth discontinuous components, is the approximation used in DE-FEM (see Eq. (7)) for a triple junction. This procedure is now generalized to an n-fold junction, as explained in the next section.

3.3. Generalization to an arbitrary number of intersecting discontinuities

The enrichment functions for an arbitrary number of intersecting discontinuities are derived by analogy and deduction from the triple junction case discussed in the previous section. The derivation of the triple junction enrichments highlights that the solution field in an element with three discontinuities meeting at a point (i.e., the triple junction) can be described by means of (36). The necessary enrichment functions for a triple junction consist of a single weak and two strong enrichment functions. To prevent linear dependency issues, one of the three potential strong enrichment functions had to be excluded, as detailed in Appendix A. In the following, this enrichment scheme is generalized to the case of an n-fold junction, where an arbitrary number n of discontinuities converge at a point.

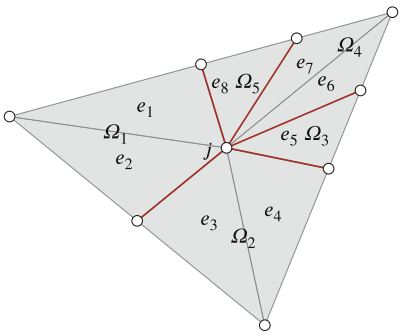

Fig. 6. A triangular domain split by five discontinuities forming a five-fold junction.

In the case of a triple junction, the weak enrichment function is characterized as a non-smooth continuous function (i.e., C^0-continuity), while the strong enrichment functions exhibit a non-smooth discontinuous function (i.e., C^{-1}-continuity). Both the weak and strong enrichments are defined by the collection of three piece-wise continuous functions, each defined within one of the subdomains generated by the intersecting discontinuities; these functions are constructed using the standard Lagrange basis functions of integration elements. In other words, the non-smooth nature of each component of the enrichment functions within its respective subdomain stems from the triangulation of the element containing the triple junction and the utilization of the basis functions associated with the triangular integration subdomains as building blocks. The enrichment functions for a domain with an arbitrary number of intersecting discontinuities at a point are defined accordingly.

As an illustrative example, the weak enrichment for the five-fold junction (i.e., $n = 5$) in Fig. 6 can be expressed as

$$\psi_i(\boldsymbol{x}) = \varphi_i(\boldsymbol{x}) \qquad \text{for } \boldsymbol{x} \in \Omega_k,\ k = \{1, \dots, n\}, \tag{37}$$

where we note that the domain Ω_k is composed of its corresponding integration subdomains—e.g., $\Omega_4 = \text{int}\left(\overline{e_6 \cup e_7}\right)$. This enrichment function, as in (32) for instance, is therefore constructed by the aid of Lagrange basis functions φ_i of their corresponding integration elements.

For the strong enrichment functions, we can generalize those defined in (34). The first strong enrichment function $\chi_{i1}(\boldsymbol{x})$, has a structure similar to $\chi_7(\boldsymbol{x})$ in (34), i.e.,

$$\chi_{i1}(\boldsymbol{x}) = \begin{cases} -\gamma_{i1}\varphi_i(\boldsymbol{x}) & \text{for } \boldsymbol{x} \in \Omega_1 = \text{int}\left(\overline{e_1 \cup e_2}\right) \\ (1-\gamma_{i1})\varphi_i(\boldsymbol{x}) & \text{for } \boldsymbol{x} \in \Omega_j,\ j = \{2, \dots, n\}. \end{cases} \tag{38}$$

The other $n-2$ strong enrichment functions are defined analogously to $\chi_8(\boldsymbol{x})$ in (34) as in

$$\chi_{ik}(\boldsymbol{x}) = \begin{cases} \varphi_i(\boldsymbol{x}) & \text{for } \boldsymbol{x} \in \cup_{j=k+1}^{n} \Omega_j, \\ 0 & \text{otherwise.} \end{cases} \tag{39}$$

Noteworthy, although χ_{ik} could also be defined in other ways, here we construct it as a special case of the original DE-FEM strong enrichment function (similarly to (38)) but with $\gamma_{ik} = 1$. The enrichment thus conforms with what we have derived in our previous section in (34). This way of defining the enrichment is also beneficial when considering a hierarchical implementation [34], where for instance branched cracks are considered as a new discontinuity meeting an existing junction.

These derivations are based on a counter-clockwise numbering of subdomains, as shown in Fig. 6. For the jumps between subdomains at the junction, two distinct scenarios arise: the jump between the last subdomain and the first subdomain, and the jumps between other adjacent subdomains at either side of the discontinuity. Referring back to Fig. 6, the latter subdomains Ω_2 to Ω_5 can be directly expressed with $\boldsymbol{\beta}_{ik}$ due to the form of the associated enrichment functions (39)—i.e., the first enrichment is continuous in Ω_2 through Ω_5. As a consequence, the jump between the last and the first subdomains is defined analogously to $\boldsymbol{\beta}_9 = \boldsymbol{\beta}_7 + \boldsymbol{\beta}_8$ in Section 3.2. Defining $[\![\boldsymbol{u}^h(\boldsymbol{x}_j)]\!]_{5,1} \equiv \boldsymbol{u}^h(\boldsymbol{x}_j)\big|_{\Omega_5} - \boldsymbol{u}^h(\boldsymbol{x}_j)\big|_{\Omega_1}$, the displacement jump is $[\![\boldsymbol{u}^h(\boldsymbol{x}_j)]\!]_{5,1} = \boldsymbol{\beta}_{i1} + \boldsymbol{\beta}_{i2} + \boldsymbol{\beta}_{i3} + \boldsymbol{\beta}_{i4}$.

In general, enrichment functions (37) to (39) are generalized for an n-fold junction by using the actual number of subdomains, i.e., by replacing 5 with n. For an n-fold junction there will thus be $n-1$ strong enrichments. The relationship between the enriched DOFs and the displacement jumps can therefore be written as

$$\boldsymbol{\beta}_{i1} = [\![\boldsymbol{u}]\!]_{1,2}, \qquad \boldsymbol{\beta}_{i2} = [\![\boldsymbol{u}]\!]_{2,3}, \qquad \cdots \qquad \boldsymbol{\beta}_{i(n-1)} = [\![\boldsymbol{u}]\!]_{n-1,n}, \qquad \sum_{k=\{1\dots n-1\}} \boldsymbol{\beta}_{ik} = [\![\boldsymbol{u}]\!]_{n,1}. \tag{40}$$

Finally, the displacement field for an n-fold junction is expressed as

$$\boldsymbol{u}^h(\boldsymbol{x}) = \underbrace{\sum_{i\in I_h} \varphi_i(\boldsymbol{x})\boldsymbol{u}_i}_{\text{standard}} + \underbrace{\overbrace{\sum_{i\in I_w} \psi_i(\boldsymbol{x})\boldsymbol{\alpha}_i}^{\text{weak}} + \overbrace{\sum_{i\in I_s}\sum_{1\le k<n} \chi_{ik}(\boldsymbol{x})\boldsymbol{\beta}_{ik}}^{\text{strong}}}_{\text{enrichment}}. \tag{41}$$

The original DE-FEM formulation is recovered in elements that do not contain a junction: in such a case there are only two subdomains, i.e., $n = 2$, and only one strong enrichment function is assigned to each enriched node.

4. Computer implementation

In this section, we discuss the computational implementation details of DE-FEM with the aid of pseudo-code. First, in Algorithm 1 we present the overall structure of an enriched finite element code. It is worth noting that the code structure does not differ significantly from a standard displacement-based finite element code. The main differences lie in the interaction between a finite element mesh and a set of discontinuities $\mathcal{D}$, which creates new enriched nodes and integration elements.

Following the structure of the algorithm, the input and initialization stages are similar to those of a standard FEM code. At this step, most of the information needed to solve the boundary value problem is loaded, typically from a file. This results in a mesh data structure consisting of a set of standard nodes, $\mathcal{N}$, and a set of elements, $\mathcal{E}$. At this stage, we also define the boundary value problem to be solved (governing partial differential equation, boundary conditions, material laws, etc.), denoted by $\mathcal{P}$ in the algorithm. We then process all the discontinuities in the set $\mathcal{D}$. To achieve this, we rely on a computational geometric engine, the details of which are beyond the scope of this work but have been thoroughly described by Zhang et al. [35]. In essence, the geometric engine identifies all original mesh elements that are intersected by the discontinuities in $\mathcal{D}$, denoted by the set $\mathcal{E}_c$, creates new enriched nodes $\mathcal{N}_e$ located at the intersections between discontinuities and edges of the mesh elements, and subdivides the cut elements into integration elements $\mathcal{E}_q$. It is worth noting that the same data structure that is used to store standard FEM nodes is augmented to accommodate for new enriched nodes. However, a more specialized data structure is needed for elements, since the original cut elements are removed (or simply masked), and new integration elements are added. A straightforward way to manage mesh elements and their integration elements is by using an ordered tree data structure [32]. It is also important to note that the geometric engine is responsible for determining the number of enriched nodes to be added.

In problems with weak discontinuities, a single enriched node is placed at every intersection between the discontinuity and the edges of finite elements, as well as at every junction. For strong discontinuities, both weak and strong enrichment nodes are placed at each intersection with the edges of an element, except at crack tips, where only a weak enrichment node is used (since there is no displacement jump at tips). This is tantamount to placing both weak and strong enriched nodes but setting the strong enriched DOFs to zero as a Dirichlet boundary condition [10]. Finally, strongly discontinuous junctions require a single weak enriched node and a number of strong enriched nodes that depend on the number of junction subdomains.

After all operations by the geometric engine have been performed, the global stiffness matrix and the global force vector are assembled. Notice that the total number of DOFs can readily be determined by the number of nodes in the set $\mathcal{N}$ and the number of DOFs per node for the given problem (e.g., d for d-dimensional elastostatics or 1 for heat conduction). The global arrays are then assembled by accounting for the contributions of all elements in the mesh. While the procedure for uncut elements follows the standard finite element method, the quadrature in integration elements requires special attention and will be discussed in detail later in this section.

Once the global stiffness matrix and the global force vector are assembled, we prescribe the boundary conditions. The degree of freedom vector is then obtained by solving the linear system of equations $\boldsymbol{KU} = \boldsymbol{F}$. With the solution vector determined, we can compute post-processing quantities such as stress, strain, among others, and write the results to an output file.

The quadrature of an integration element is described in Algorithm 2, where we denote the integration element as $e_{\diagdown}$ and the parent cut element as e. It is important to note that each element has its own isoparametric mapping and therefore we need to select carefully the appropriate components for the numerical quadrature. In essence, the standard shape function vector and the strain–displacement matrix of the parent element are augmented by the contributions of weak and strong enrichment functions. This procedure ensures that the augmentation is performed correctly while also conducting integration on the (smaller) integration element. Therefore, the determinant of the Jacobian matrix of the integration element is used.

Making reference to Algorithm 2, we first determine the element DOF table which is used to map local elements of the arrays to their actual locations in the global stiffness matrix and force vector. To achieve this we can simply use the IDs of the mesh nodes of the parent cut element e and those of the enriched nodes of the integration element. Note that the number of enriched nodes in an integration element will depend on the types of discontinuities and whether the integration element belongs to a fully split parent element or one containing a junction. With the element DOF table, we determine the total number of local DOFs n, which is then used to initialize the local stiffness matrix and the local force vector. The nodal coordinates of both the integration and the parent cut elements are needed to compute quantities related to their corresponding mappings, namely the inverse of the Jacobian matrix and its determinant.

We use standard Gauss quadrature with weights $\boldsymbol{\gamma}$ and coordinates $\boldsymbol{\xi}$, and therefore we start a loop over the total number of Gauss quadrature points n_{GP}. Within the loop, we can discriminate operations related to the integration element and those related to the parent element. Regarding operations related to the integration element, we first compute the Lagrange shape functions and

Algorithm 1 Structure of an enriched finite element code

Input: A file handle f_{in} with input data, which includes mesh data (i.e., set of nodes $\mathcal{N}$ and elements $\mathcal{E}$), boundary value problem data $\mathcal{P}$ (equation to be solved, boundary conditions, constitutive laws, material properties, etc.), and a discontinuity set D

function EnrichedFEM
- *– input and initialization stage*
- $\{\mathcal{N}, \mathcal{E}, \mathcal{P}\} \leftarrow$ ReadInput(f_{in}) *– get nodes, elements, and BVP data*
- *– process discontinuities*
- **for** $d_i \in D$ **do** *– loop over discontinuities*
  - $\mathcal{E}_c \leftarrow$ Intersect$(\mathcal{E}_c, d_i)$ *– find cut elements*
  - $\{\mathcal{N}_e, \mathcal{E}_q\} \leftarrow$ GeometricEngine$(\mathcal{E}_c, d_i)$ *– create enriched nodes and integration elements*
  - $\mathcal{N} \leftarrow \mathcal{N} \cup \mathcal{N}_e$ *– add enriched nodes*
  - $\mathcal{E} \leftarrow (\mathcal{E} \setminus \mathcal{E}_c) \cup \mathcal{E}_q$ *– mask cut elements and add integration elements*
- *– assembly stage*
- $n_D \leftarrow |\mathcal{N}| \times$ DOFsPerNode$(\mathcal{P})$ *– get total number of DOFs*
- $\{\boldsymbol{K}, \boldsymbol{F}\} \leftarrow \left\{\mathbf{0}_{n_D \times n_D}, \mathbf{0}_{n_D \times 1}\right\}$ *– initialize global array data structures*
- **for** $e \in \mathcal{E}$ **do**
  - $\{\boldsymbol{k}_e, \boldsymbol{f}_e, \mathcal{F}\} \leftarrow$ Quadrature$(e, \mathcal{N}, \mathcal{P})$ *– obtain local element arrays and EFT*
  - $\boldsymbol{K} \leftarrow$ Assemble$\left(\boldsymbol{k}_e, \mathcal{F}\right)$ *– assemble contribution to stiffness matrix*
  - $\boldsymbol{F} \leftarrow$ Assemble$\left(\boldsymbol{f}_e, \mathcal{F}\right)$ *– assemble contribution to force vector*
- *– solution stage*
- $\{\boldsymbol{K}, \boldsymbol{F}\} \leftarrow$ PrescribeBCs$(\boldsymbol{K}, \boldsymbol{F})$ *– apply boundary conditions*
- $\boldsymbol{U} \leftarrow \boldsymbol{K}^{-1}\boldsymbol{F}$ *– solve for unknown field*
- *– post-process solution and output*
- $\{\boldsymbol{\sigma}, \boldsymbol{\epsilon}, \ldots\} \leftarrow$ PostProcess$(\boldsymbol{U})$ *– get stress, strain, and other quantities*
- $f_{\text{out}} \leftarrow$ WriteOutput$(\mathcal{N}, \mathcal{E}, \boldsymbol{U}, \boldsymbol{\sigma}, \boldsymbol{\epsilon}, \ldots)$ *– write results to file*

end function

their derivatives with respect to master coordinates, the inverse of the Jacobian matrix, and its determinant. These are then used to compute the enrichment functions and their derivatives through a loop over enriched node locations. Noteworthy, at each location $\boldsymbol{x}_e$ there is a single weak enrichment and a single strong enrichment, unless the location is that of a junction—in which case there is a single weak enrichment but multiple strong enrichments. It is also worth noting that enrichment functions can be multiplied by scaling factors γ_w and γ_s, which help control the condition number of stiffness matrices when discontinuities lie arbitrarily close to standard mesh nodes [27–29]. The inverse of the Jacobian matrix corresponding to the integration element is then used to compute the derivatives of the enrichment functions with respect to global coordinates.

Once computed, enrichment functions and their derivatives are expanded and added to arrays $\boldsymbol{\Phi}$ and $\boldsymbol{B}$, respectively. In the pseudo-code, the expansion to account for multiple DOFs is done for the shape function array $\boldsymbol{\Phi}$ by means of the Kronecker product, denoted by the symbol $\odot$. Also, $\boldsymbol{\Delta}\left(\boldsymbol{\nabla}_{\boldsymbol{x}}\psi_e\right)$ is used to denote the proper arrangement of the derivatives in the strain–displacement matrix; for instance, when using Voigt notation in 2-D we have

$$\boldsymbol{\Delta}\left(\boldsymbol{\nabla}_{\boldsymbol{x}}\psi_e\right) = \begin{bmatrix} \frac{\partial \psi_e}{\partial x} & 0 \\ 0 & \frac{\partial \psi_e}{\partial y} \\ \frac{\partial \psi_e}{\partial y} & \frac{\partial \psi_e}{\partial x} \end{bmatrix}.$$

Once the matrices $\boldsymbol{\Phi}$ and $\boldsymbol{B}$ contain all elements corresponding to enriched functions and their derivatives, respectively, we proceed with operations at the parent cut element e. First, we find the master coordinate $\boldsymbol{\xi}_p$ corresponding to the global coordinate $\boldsymbol{x} = \boldsymbol{X}_{\!\text{e}}^{\top}\boldsymbol{\varphi}_{\!\text{e}}^{\top}$. Once this is known, the shape functions of the parent element and their derivatives are determined as in standard FEM and are subsequently added to the corresponding arrays.

Algorithm 2 Numerical quadrature in integration elements

Input: Triangular integration element $e_\triangle$, parent element e, node set $\mathcal{N}$, and problem data $\mathcal{P}$, number of integration points n_{GP}
Output: Local element arrays $\boldsymbol{k}_e$, $\boldsymbol{f}_e$, and element freedom table $\mathcal{F}$

function QUADRATURE
- $C \leftarrow$ CONNECTIVITY(e) – *get standard and enriched node IDs*
- $\mathcal{F} \leftarrow$ DOFS$(C,$ DOFSPERNODE$(\mathcal{P}))$ – *get element freedom table*
- $n \leftarrow |\mathcal{F}|$ – *get total number of local DOFs*
- $\{\boldsymbol{k}_e, \boldsymbol{f}_e\} \leftarrow \{\boldsymbol{0}_{n\times n}, \boldsymbol{0}_{n\times 1}\}$ – *initialize local arrays*
- $\boldsymbol{X}_\triangle^\top \leftarrow \begin{bmatrix} x_1 & x_2 & x_3 \\ y_1 & y_2 & y_3 \end{bmatrix}$ – *get nodal coordinates of integration element*
- $\boldsymbol{X}^\top \leftarrow \begin{bmatrix} x_1 & x_2 & x_3 \\ y_1 & y_2 & y_3 \end{bmatrix}$ – *get nodal coordinates of parent element*
- *– loop over integration points*
- $\{\boldsymbol{w}, \boldsymbol{\xi}\} \leftarrow$ QUADRATURERULE(n_{GP}) – *weights and master coordinates*
- **for** $i \leftarrow \{1 \dots n_{\text{GP}}\}$ **do**
  - $\boldsymbol{\Phi} \leftarrow \varnothing$ – *shape function array*
  - $\boldsymbol{B} \leftarrow \varnothing$ – *strain-displacement array*
  - *– operations related to integration element*
  - $\{\boldsymbol{\varphi}_\triangle, \boldsymbol{\nabla}_\xi \boldsymbol{\varphi}_\triangle\} \leftarrow$ SHAPES $(\boldsymbol{\xi}_i, e_\triangle)$ – *get Lagrange shape functions/derivatives*
  - $\{\boldsymbol{J}_\triangle^{-1}, j_\triangle\} \leftarrow$ JACOBIAN $(\boldsymbol{X}_\triangle, \boldsymbol{\nabla}_\xi \boldsymbol{\varphi}_\triangle)$ – *Jacobian inverse and determinant*
  - $\boldsymbol{x} \leftarrow \boldsymbol{X}_\triangle^\top \boldsymbol{\varphi}_\triangle^\top$ – *compute global coordinate*
  - *– loop over enrichments*
  - **for** $\{\boldsymbol{x}_e\} \in \mathcal{N}_e \cap e_\triangle$ **do**
    - $\{\gamma_w, \gamma_s\} \leftarrow$ GETWEIGHTS $(\boldsymbol{x}_e, e_\triangle)$ – *get scaling factors*
    - $\{\psi_e, \boldsymbol{\nabla}_\xi \psi_e\} \leftarrow$ WEAK $(\gamma_w, \boldsymbol{\varphi}_\triangle, \boldsymbol{\nabla}_\xi \boldsymbol{\varphi}_\triangle)$ – *weak enrichments/derivatives*
    - $\{\chi_e, \boldsymbol{\nabla}_\xi \chi_e, \} \leftarrow$ STRONG $(\gamma_s, \boldsymbol{\varphi}_\triangle, \boldsymbol{\nabla}_\xi \boldsymbol{\varphi}_\triangle)$ – *strong enrichments/derivatives*
    - $\{\boldsymbol{\nabla}_x \psi_e, \boldsymbol{\nabla}_x \chi_e, \} \leftarrow \{\boldsymbol{J}_\triangle^{-1} \boldsymbol{\nabla}_\xi \psi_e, \boldsymbol{J}_\triangle^{-1} \boldsymbol{\nabla}_\xi \chi_e\}$ – *derivatives w.r.t. global coordinates*
    - $\boldsymbol{\Phi} \leftarrow \begin{bmatrix} \boldsymbol{\Phi} & \psi_e \odot \boldsymbol{I} & \chi_e \odot \boldsymbol{I} \end{bmatrix}$ – *stack enrichment functions*
    - $\boldsymbol{B} \leftarrow \begin{bmatrix} \boldsymbol{B} & \boldsymbol{\Delta}(\boldsymbol{\nabla}_x \psi_e) & \boldsymbol{\Delta}(\boldsymbol{\nabla}_x \chi_e) \end{bmatrix}$ – *stack derivatives*
  - *– operations involving parent element*
  - $\boldsymbol{\xi}_p \leftarrow$ INVERSEMAPPING$(\boldsymbol{x})$ – *find master coordinate*
  - $\{\boldsymbol{\varphi}, \boldsymbol{\nabla}_\xi \boldsymbol{\varphi}\} \leftarrow$ SHAPES $(\boldsymbol{\xi}_p, e)$ – *shape functions/derivatives*
  - $\boldsymbol{J}^{-1} \leftarrow$ JACOBIAN$(\boldsymbol{X}, \boldsymbol{\nabla}_\xi \boldsymbol{\varphi})$ – *Jacobian inverse*
  - $\boldsymbol{\nabla}_x \boldsymbol{\varphi} \leftarrow \boldsymbol{J}^{-1} \boldsymbol{\nabla}_\xi \boldsymbol{\varphi}$ – *derivatives w.r.t. global coordinates*
  - $\boldsymbol{\Phi} \leftarrow \begin{bmatrix} \boldsymbol{\Phi} & \boldsymbol{\varphi} \odot \boldsymbol{I} \end{bmatrix}$ – *stack enrichment functions*
  - $\boldsymbol{B} \leftarrow \begin{bmatrix} \boldsymbol{B} & \boldsymbol{\Delta}(\boldsymbol{\nabla}_x \boldsymbol{\varphi}) \end{bmatrix}$ – *stack derivatives*
  - *– add contributions to local arrays*
  - $\boldsymbol{C} \leftarrow$ CONSTITUTIVE $(\boldsymbol{x})$ – *constitutive law*
  - $\boldsymbol{k}_e \leftarrow \boldsymbol{k}_e + w_i\, j_\triangle\, \boldsymbol{B}^\top \boldsymbol{C}\, \boldsymbol{B}$ – *update stiffness matrix*
  - $\boldsymbol{f}_e \leftarrow \boldsymbol{f}_e + w_i\, j_\triangle\, \boldsymbol{\Phi}^\top \boldsymbol{b}$ – *update force vector*
- **return** $\{\boldsymbol{k}_e, \boldsymbol{f}_e, \mathcal{F}\}$

end function

Finally, we add the contribution of the Gauss integration point to the local stiffness matrix (for which the constitutive matrix $\boldsymbol{C}$ is evaluated) and the local force vector. The function returns these arrays along with the element DOF table, which is required to properly integrate their contributions into their global counterparts. It is worth noting that the primary difference from the original DE-FEM implementation is the need to determine the number of enrichments at a junction based on the number of junction subdomains. This can be achieved straightforwardly through the correct bookkeeping strategy.

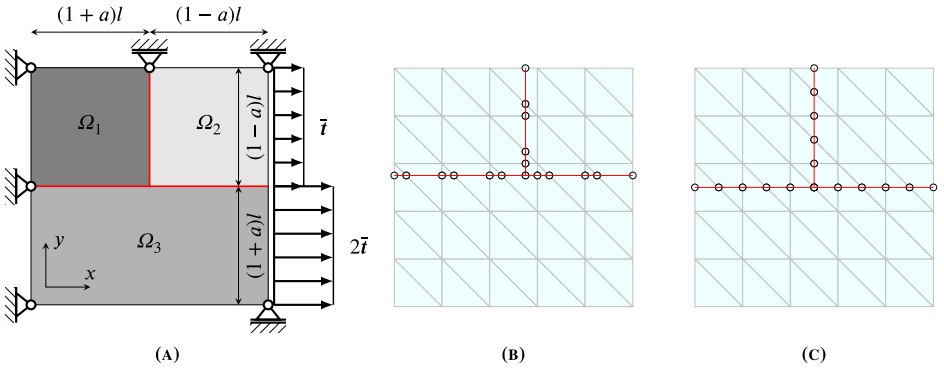

Fig. 7. Discontinuous patch test (A). The same structured discretization (5 × 5 triangulated rectangular grid) is employed in (B), where the triple junction is located within an element ($a = 0.1$), and in (C), where it is placed on an element edge ($a = 0$). Each circle in (B, C) represents the location of an enriched node defined at the intersection between a discontinuity line and an element edge, as well as at the intersection between the two discontinuities.

5. Numerical examples

DE-FEM's performance and capability in handling problems with multiple discontinuities meeting at a point are investigated through several numerical examples. For elastostatics problems, we assume a plane strain linear elastic material behavior under the assumption of small deformations. Across discontinuities, we assume either perfectly bonded domains as in the three-material wedge example in Section 5.2, linear elastic behavior governed by a cohesive law—leading to elastic interface behavior in the discontinuity cohesive patch test in Section 5.1 and sliding grain boundaries in the anelasticity of polycrystalline material example in Section 5.4—or a traction-free interface as in the branched crack examples in Section 5.3. For the heat conduction application in Section 5.5, the bulk material has constant thermal conductivity, and discontinuities behave as material interfaces. This indicates that both weak and strong enrichments are employed in the examples in Sections 5.1, 5.3, and 5.4, whereas only the weak enrichment was used in the examples in Sections 5.2 and 5.5.

Unless otherwise stated, quantities are dimensionless so they can be understood under any consistent unit system, and domains are discretized using structured meshes of linear triangular elements similar to those depicted in Fig. 7.

5.1. Discontinuous cohesive patch test

This test demonstrates the effectiveness of the proposed enrichment scheme in reproducing independent strain fields across discontinuities and around a junction irrespective of the discretization. Consider in Fig. 7(a) a square plate of size $2l$ ($l = 1$) divided into three subdomains Ω_i by discontinuities Γ_{ij} ($i, j = \{1, 2, 3\}$). Each subdomain has elastic modulus $E_i = 10i$ and Poisson's ratio $\nu_i = 0$. The test is designed to produce independent horizontal elongations in the upper ($\Omega_1 \cup \Omega_2$) and lower (Ω_3) blocks of the plate. To this end, the plate is constrained by prescribing $\boldsymbol{u}(0, y) = \mathbf{0}$ to the left edge, $u_y(2l, y) = 0$ to the right-edge, and $u_y(l, y) = 0$ to the mid-side node on the upper edge. These boundary conditions are prescribed using standard procedures for both standard and enriched DOFs, since the latter are also zero. Tractions $\bar{\boldsymbol{t}} = 1\boldsymbol{e}_x$ and $2\bar{\boldsymbol{t}}$ are applied to the top and bottom sides of the right edge as shown in Fig. 7(a). A linear elastic cohesive law is used along interfaces between subdomains. For discontinuity Γ_{12}, tangential and normal stiffnesses are $t_{tt} = 0$ and $t_{nn} = 10$, respectively. Normal and tangential stiffnesses along discontinuities Γ_{13} and Γ_{23} are set to zero.

To evaluate the necessity of incorporating both weak and strong enrichment functions, we conducted a test where weak enrichment functions are excluded. Figs. 8(c) and 8(d) show the contour plots of the strain field in the deformed configuration. It is apparent that while the discontinuous displacement field can be reproduced to some extent (though inaccurately when the discontinuity is placed within an element), the strain field cannot be reproduced. In contrast, as illustrated in Figs. 8(a) and 8(b), incorporating both weak and strong enrichment functions enables the accurate reproduction of the expected solution, irrespective of the location of the junction (i.e., within an element or along an element edge). This solution corresponds to three distinct strain fields in Ω_1, Ω_2, and Ω_3, with values $\bar{t}_x/E_1 = 1/10$, $\bar{t}_x/E_2 = 1/20$, and $2\bar{t}_x/E_3 = 1/15$, respectively. Notably, we show the strain field rather than the stress field to emphasize the jump in strain at the upper part of the domain (plotting the stress would have resulted in a uniform field). Furthermore, the figure shows both displacement and gradient jumps, demonstrating that our proposed enrichment scheme effectively reproduces independent kinematic fields.

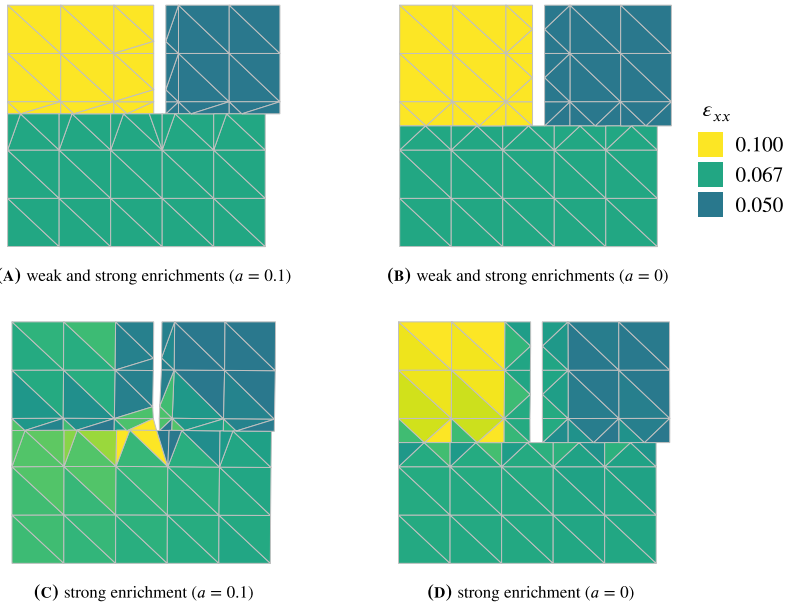

(A) weak and strong enrichments ($a = 0.1$) **(B)** weak and strong enrichments ($a = 0$)

(C) strong enrichment ($a = 0.1$) **(D)** strong enrichment ($a = 0$)

Fig. 8. Strain field superimposed on the deformed configuration obtained with the proposed DE-FEM formulation, which comprises both weak and strong enrichments (A, B), and contrasted with a solution that neglects the weak enrichments (C, D). Integration elements are also plotted for post-processing purposes. The discretization used is shown in Fig. 7.

5.2. Convergence analysis for a three-material wedge problem

The convergence properties of the method are now investigated. An infinite plate with three wedge regions, perfectly bonded to one another, is analyzed by prescribing the asymptotic displacement field as essential boundary conditions on the computational square domain shown in Fig. 9(a). The actual displacement field values correspond to $K_{\mathrm{I}} = K_{\mathrm{II}} = 1$, i.e., identical mode I and mode II stress intensity factors (SIFs), as described by Akhondzadeh et al. [36].

The square plate domain of size $l = 4$ consists of three different materials with elastic modulus $E_i = 10^{i-1}$ for the ith subdomain and equal Poisson's ratio $\nu = 0.3$. Fig. 9 shows the meshes used to obtain the first points in the error curves reported in Fig. 10 for unfitted DE-FEM and fitted FEM discretizations. Across two neighboring domains, the displacement field remains continuous (due to the perfect bonding between the wedges), albeit with discontinuous field gradients. The continuous nature of the displacement field across a material interface allows us to either disregard or set the values of the DOFs associated with strong enrichment functions to zero. In this case, we disregard them and employ only the weak enrichment.

For the enforcement of essential boundary conditions on the weak enrichment DOFs located on the boundary, the boundary condition values are obtained by solving a local problem as discussed in Section 2. Due to the test configuration, the analytical solution presents a strain singularity at the junction point.

The convergence properties of DE-FEM are demonstrated by computing the error of the approximate solution $\boldsymbol{u}^h$ with respect to the analytical solution $\boldsymbol{u}$ in the energy norm, according to

$$\frac{\|\boldsymbol{u} - \boldsymbol{u}^h\|_{\mathcal{E}(\Omega)}}{\|\boldsymbol{u}\|_{\mathcal{E}(\Omega)}} = \frac{\sqrt{\int_\Omega (\boldsymbol{\varepsilon} - \boldsymbol{\varepsilon}^h)^\top \boldsymbol{C} (\boldsymbol{\varepsilon} - \boldsymbol{\varepsilon}^h)\, \mathrm{d}\Omega}}{\sqrt{\int_\Omega \boldsymbol{\varepsilon}^\top \boldsymbol{C} \boldsymbol{\varepsilon}\, \mathrm{d}\Omega}}, \tag{42}$$

with $\boldsymbol{\varepsilon}^h$ and $\boldsymbol{\varepsilon}$ their corresponding strain tensors, and $\boldsymbol{C}$ is the tensor of elastic constants.

Convergence results are summarized in Fig. 10. Convergence rates obtained for DE-FEM and standard FEM using structured meshes are 0.35 and 0.32, respectively. For unstructured meshes, the convergence rates for DE-FEM and standard FEM are 0.40 and 0.35, respectively. It is worth noting that, while the optimal convergence rate of 0.5 is not attained, the results obtained follow closely those of standard FEM on fitted meshes. The low convergence rate is attributed to the fact that the enrichment functions employed in this work only capture the kinematics of the discontinuities and therefore cannot reproduce the singularity at the junction.

5.3. Branched cracks

A series of illustrative cases, inspired by those reported by Daux et al. [6], are solved to showcase the modeling capability of DE-FEM in accurately generating results for any number of branched cracks. Initially, the focus is on branched cracks. Subsequently, two specific scenarios involving cross-shaped and star-shaped cracks are examined. Results are obtained with Young's modulus and Poisson's ratio taken as 10.0 and 0.0, respectively. Additionally, the magnitude of the normal traction vector is set to one.

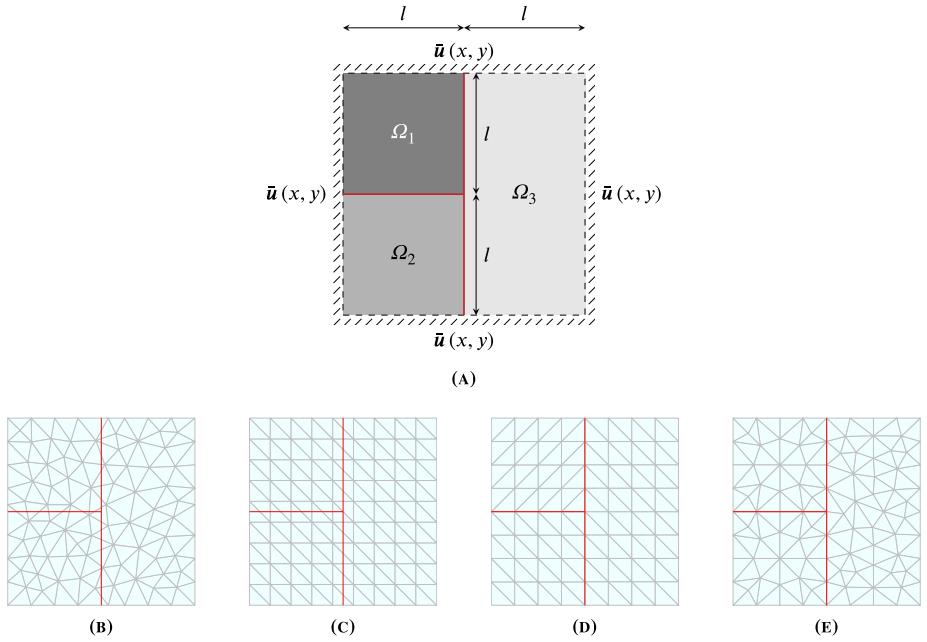

Fig. 9. (A) Three-material wedge problem: geometry and boundary conditions; DE-FEM discretizations with unfitted (B) unstructured and (C) structured meshes; FEM discretizations with fitted (D) structured and (E) unstructured meshes. The first points of each line in Fig. 10 have been obtained using these discretizations.

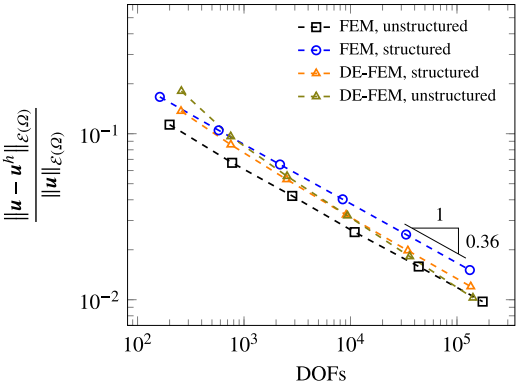

Fig. 10. Convergence of the relative error of the energy norm with respect to the number of DOFs using structured and unstructured meshes.

5.3.1. *Symmetric branched crack*

To assess the accuracy of DE-FEM regarding the calculation of stress intensity factors, we study a symmetric branched crack in an infinite plate subject to uniaxial loading perpendicular to the axis of symmetry. Geometry and boundary conditions of the computational domain are reported in Fig. 11. We first consider a configuration with $l = 16$, $w = 20$, $a = b = 1$ and $\theta = \pi/4$. While the solution obtained with a semi-analytical approach is available for an infinite domain [37], we follow Daux et al. [6] and take a sufficiently large rectangular domain for the analysis. Since the dimensions of this domain substantially exceed the length of the crack branches, it effectively functions as a representative model of an infinite plate.

The normalized SIFs at crack tips A and B are computed as

$$\overline{K}_{\mathrm{I}}^{A} = K_{\mathrm{I}}^{A}/\sigma\sqrt{\pi c}, \qquad \overline{K}_{\mathrm{I}}^{B} = K_{\mathrm{I}}^{B}/\sigma\sqrt{\pi c}, \qquad \overline{K}_{\mathrm{II}}^{B} = K_{\mathrm{II}}^{B}/\sigma\sqrt{\pi c}, \tag{43}$$

where K_{I} and K_{II} are the calculated mode I and II SIFs, respectively (refer to the procedure outlined in § 2.5 of Aragón and Simone [10]). Table 1 presents the results of a mesh refinement study conducted using DE-FEM with unstructured graded meshes of linear triangular elements, an example of which is shown in Fig. 11. These results are compared to those obtained by Daux et al. [6]

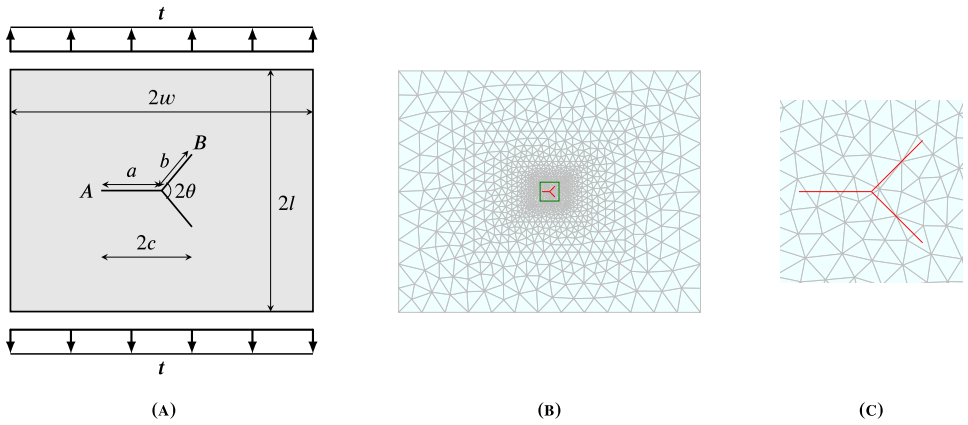

Fig. 11. (A) Symmetric branched crack in a plate subject to uniaxial tension [6] ($l = 16$, $w = 20$, $a = b = 1$, $\theta = \pi/4$; crack not to scale); (B) underlying unstructured graded mesh used to obtain the first column of results in Table 1 with mesh size $h/a = 0.25$ and (C) zoomed view around the crack.

Table 1
DE-FEM normalized SIFs for various values of the ratio h/a (h is the mesh size around the crack).

	h/a						
	0.25	0.21	0.18	0.09	0.05	0.05 (XFEM [6])	*
$\overline{K}_{\mathrm{I}}^{A}$	1.0384	1.0385	1.0400	1.0446	1.0451	1.044	1.044
$\overline{K}_{\mathrm{I}}^{B}$	0.4949	0.4986	0.4989	0.4981	0.4959	0.496	0.495
$\overline{K}_{\mathrm{II}}^{B}$	0.5018	0.5081	0.5089	0.5091	0.5091	0.508	0.506

* Reference solution by Chen and Hasebe [37, Table 4].

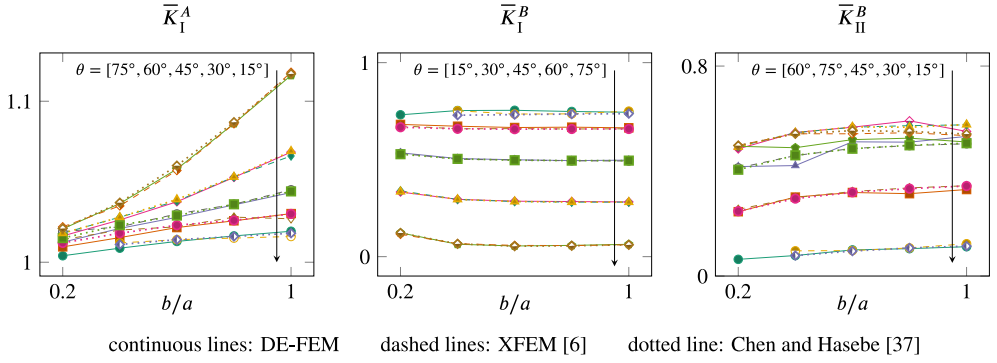

Fig. 12. Normalized SIFs at points A (left) and B (middle,right) for the branched crack problem in Fig. 11, and for various ratios of b/a and branched angles θ.

using XFEM with an unstructured mesh refined around the crack and to the results by Chen and Hasebe [37] obtained using a semi-analytical approach. We notice that the normalized SIFs converge to the reference values as the mesh is refined; acceptable results can be obtained even with coarse discretizations.

While the results in Table 1 are obtained for a fixed value of a, Fig. 12 shows the normalized SIFs for varying values of b/a and the branching angle θ, namely $a/b = [0.2, 0.4, 0.6, 0.8, 1.0]$ and $\theta = [15°, 30°, 45°, 60°, 75°]$. The results, also tabulated in Appendix C (Table 2), are compared to those obtained numerically via XFEM by Daux et al. [6] (dashed lines) and by Chen and Hasebe [37] (dotted lines) using a semi-analytical approach. It is worth noting that our results are in good agreement to those obtained by XFEM that uses singular enrichments around crack tips.

5.3.2. Cross- and star-shaped cracks

To illustrate the ability of the method to accurately represent discontinuous fields around intersecting cracks in more complex scenarios, the plates with cross- and star-shaped cracks in Fig. 13 are analyzed. Both problems are solved using structured discretizations with an equal number of elements in the vertical and horizontal directions, employing a 51 × 51 triangulated rectangular grid. This discretization is similar to that used by Daux et al. [6], who employed a uniform mesh of 40 × 40 bilinear quadrilateral elements to solve the star-shaped crack problem. Due to the regular distribution of mesh points and the geometry

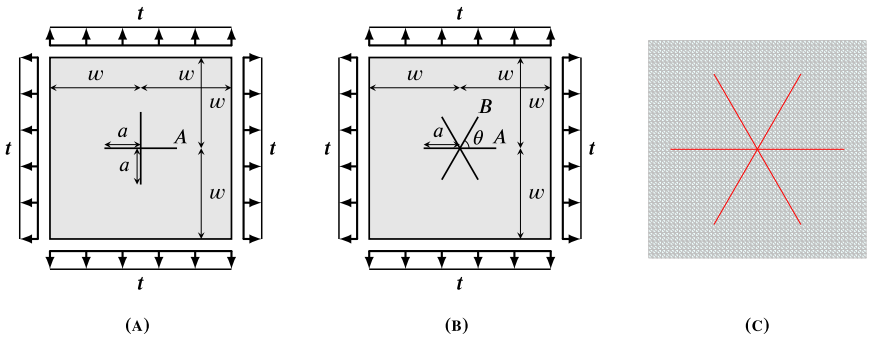

Fig. 13. Cross-shaped (A) and star-shaped ($\theta = \pi/3$) (B) crack problems, along with (C) the underlying 51 × 51 triangulated rectangular grid for the $a/w = 0.8$ configuration of the star-shaped crack problem in (B). The same background mesh is used for the cross-shaped crack problem in (A).

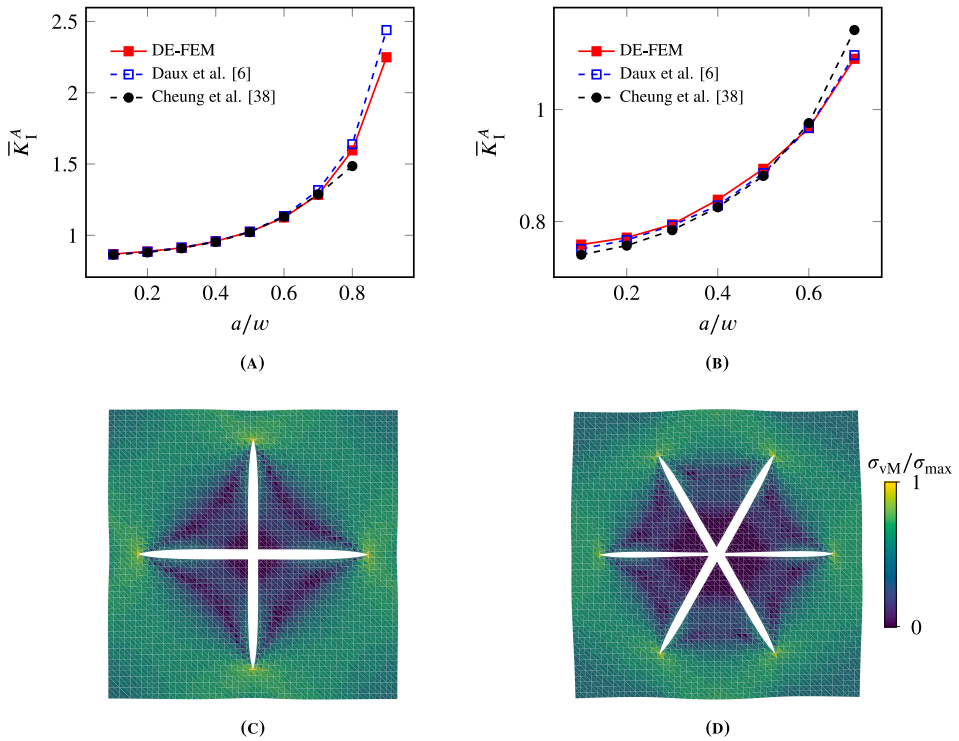

Fig. 14. Stress intensity factor $\overline{K}_I^A$ (top) as a function of the crack length to specimen size ratio a/w, and normalized von Mises stress on the deformed configuration (bottom) for the cross-shaped cracks (A, C) and the star-shaped cracks (B, D) with $a/w = 0.8$. The results are obtained using a structured discretization (51 × 51 triangulated rectangular grid).

of the cracks (see Fig. 13(c)), the junction is located along an element edge in both cases, similar to the one clearly depicted in Fig. 7(c).

The normalized SIFs at crack tip A, $\overline{K}_I^A = K_I^A/\sigma\sqrt{\pi a}$, are shown in Figs. 14(a) and 14(b) for various ratios a/w. These results are also tabulated in Appendix C (Tables 3 and 4). DE-FEM results closely resemble those obtained with a semi-analytical approach by Cheung et al. [38] and numerical results obtained with XFEM by Daux et al. [6]. Additionally, the von Mises stress field (normalized by the maximum stress) is also illustrated on the deformed configuration for $a/w = 0.8$ in Figs. 14(c) and 14(d).

5.4. Freely sliding grain boundaries in polycrystalline material

We now show an application of DE-FEM to a polycrystalline material composed of regular hexagonal grains. This example was first proposed by Ghahremani [39] and studied by Simone et al. [7] using GFEM on the periodic unit cell shown in Fig. 15(a). Grain boundary sliding is the primary mechanism behind the anelastic deformation of polycrystalline materials. When these materials are subject to constant stress over time and at high temperatures, failure occurs along grain boundaries. At low stress levels, as

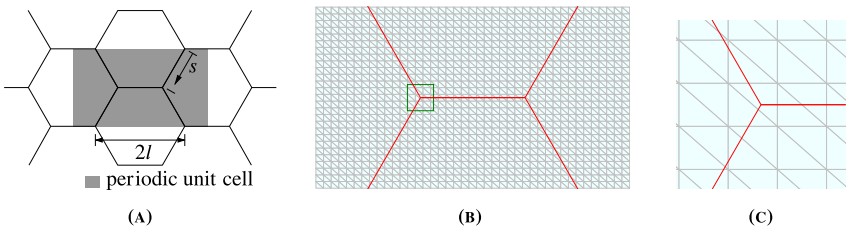

Fig. 15. (A) Periodic unit cell used in the grain boundary sliding example: l is the side length of a grain, s is the relative location along the grain boundary, and $L = 3l$ is the length of the unit cell; (B) one of the structured discretizations (41 × 27 triangulated rectangular grid) used to obtain the results in Fig. 16 and (C) zoomed view around a triple junction.

a limiting case, individual grains behave elastically, the viscous resistance of grain boundaries can be neglected, and they can be effectively considered as freely sliding against each other. In this so-called "relaxed state", a body has lower rigidity compared to the unrelaxed state, where shear tractions are transmitted across the grain boundaries. The relaxed Young's modulus is, therefore, a key parameter in predicting these time-dependent deformations.

In the spirit of DE-FEM [10], the periodic unit cell domain is discretized using a structured mesh of linear triangular elements, a typical example of which is shown in Fig. 15(b). Discontinuities, representing grain boundaries, are decoupled from the discretization, as illustrated in Fig. 15(c). To enable free boundary sliding, we employ a linear elastic cohesive law that governs the interaction between neighboring grains. The cohesive law comprises tangential and normal stiffness parameters denoted as t_{tt} and t_{nn}, respectively. We set $t_{\mathrm{tt}} = 0$ to enable unrestricted sliding between grains, while $t_{\mathrm{nn}} = 5 \times 10^4$ is chosen to prevent grain separation. These cohesive law parameters ensure that grains can freely slide past each other while remaining connected. We consider the polycrystalline aggregate to be composed of linear elastic grains with Young's modulus $E = 10$. The application of periodic boundary conditions is achieved using the methodology outlined in Appendix D.

To verify the accuracy of our approach, we compute the relaxed Young modulus

$$\bar{E} = \left(\frac{\bar{\epsilon}_x}{\bar{\sigma}_x} + \frac{\nu^2}{E} \right)^{-1}, \tag{44}$$

of the unit cell subject to uniaxial tension and compare the results with those obtained using GFEM [7] and with the findings reported by Ghahremani [39]. In (44) $\bar{\epsilon}_x$ and $\bar{\sigma}_x$ represent relaxed strain and stress values in the horizontal direction, respectively. As we impose a unit horizontal displacement along the right boundary, the relaxed strain $\bar{\epsilon}_x$ is calculated as $1/L$, where L denotes the length of the unit cell. The relaxed stress $\bar{\sigma}_x$ is determined as the horizontal component of the resultant reaction force along the right boundary divided by the cross-sectional area A. The cross-sectional area is simply the product of the thickness (equal to unity) and the height of the unit cell.

Fig. 16(a) shows the normalized relaxed Young's modulus $\bar{E}/E$ for different discretizations and across a range of Poisson's ratio values. The results exhibit a good agreement with those reported by Ghahremani [39] and Simone et al. using GFEM [7]. The local response in terms of tangential displacement jump $[\![u_s]\!]$ along an inclined grain boundary is reported for $\nu = 0.3$ in Fig. 16(b). The results, similar to those obtained with GFEM [7], indicate that both methods quickly converge to the same displacement profile. Lastly, the normalized von Mises stress is depicted in Fig. 17. Upon comparing it with the GFEM solution, a similar pattern is observed, with some minor differences at certain locations. Apart for the different enrichment approaches in DE-FEM and GFEM, the differences between results, seen in Figs. 16 and 17, can also be attributed to the different discretizations used in the two methods. Both methods employ a structured $m \times n$ discretization of the rectangular unit cell; in DE-FEM each grid element is split into two triangular elements, whereas in GFEM bilinear quadrilateral elements are used.

5.5. Heat conduction in a polycrystalline material

The last application deals with the heat conduction problem in the polycrystalline aggregate depicted in Fig. 18(a). This problem was studied by Aragón et al. [8]. A polycrystalline material is subject to a uniform heat flux $\bar{q} = 100$ W/m on the top edge, while the bottom edge serves as a convective boundary and the vertical edges are insulated. For the convective boundary, the ambient temperature and heat transfer coefficient are set to 293 K and 100 W/(m K), respectively. The grains have different conductivity values equal to (in W/(m K)) $k_1 = 2$, $k_2 = 4$, $k_3 = 8$, and $k_4 = 380$. As these grains are perfectly bonded to each other, no temperature discontinuities are present; therefore, only the weak enrichment function has been utilized. Figs. 18(b) and 18(c) show the discretized domain and zoomed views around representative junctions. The resulting temperature field is plotted in Fig. 19(a) and mirrors the result obtained via GFEM [8].

6. Summary and conclusions

In this work we introduced a discontinuity-enriched finite element method for modeling an arbitrary number of intersecting discontinuities. Our approach, which uses enrichments only to address the kinematics of both weak and strong discontinuities

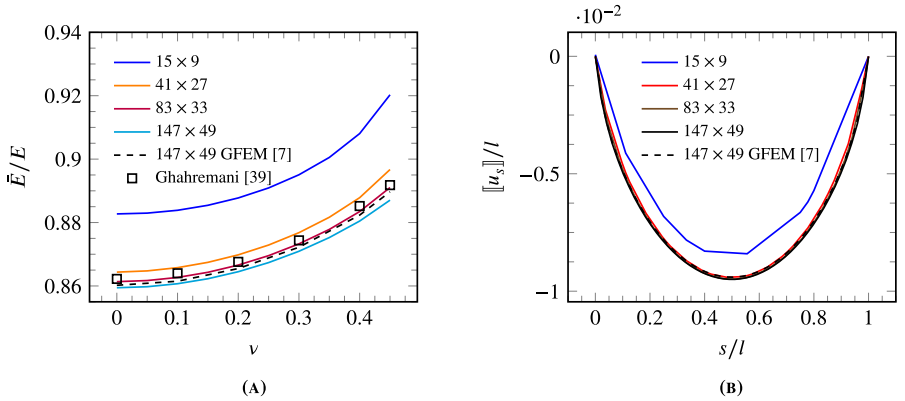

Fig. 16. Mesh convergence of (A) the variation of the relative normalized relaxed modulus with respect to the Poisson's ratio, and (B) the displacement jump in the tangential direction along an inclined grain boundary ($\nu = 0.3$).

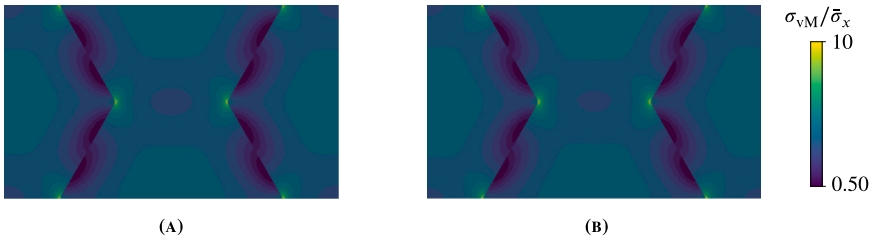

Fig. 17. Normalized von Mises stress field $\sigma_{\mathrm{vM}}/\bar{\sigma}_x$ ($\nu = 0.3$): (A) DE-FEM and (B) GFEM [7] results are obtained using a structured 240 × 136 discretization of the rectangular unit cell.

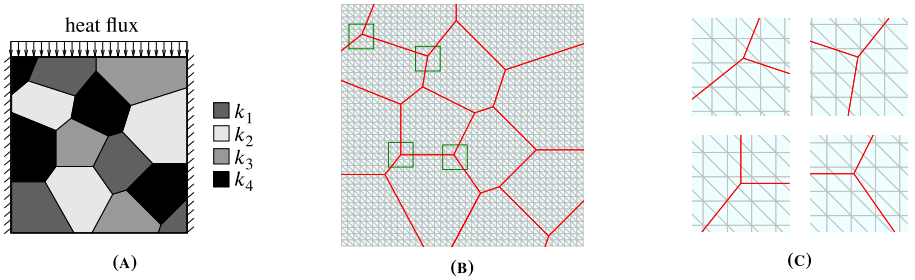

Fig. 18. (A) Heat conduction problem in a polycrystalline material. (B) Simulation domain consisting of a 39 × 39 triangulated rectangular structured grid. (C) Green squares in (B) annotate specific junctions; the junctions are reported in the same order, starting from the bottom left box and proceeding in a clockwise direction. (For interpretation of the references to color in this figure legend, the reader is referred to the web version of this article.)

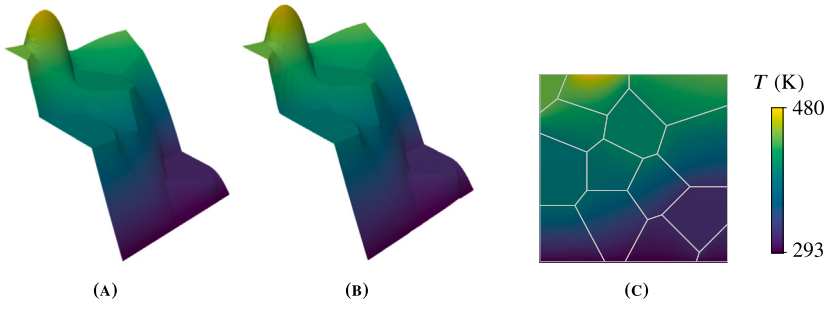

Fig. 19. The DE-FEM temperature distribution (A) matches the field reported in (B) from Aragón et al. [8] using GFEM. (C) The flattened view of the reference solution does not clearly reveal the discontinuous temperature gradients along grain boundaries, which are visible in the three-dimensional renderings in (A) and (B).

with a three-term unified formulation, is effective in addressing weak discontinuities in material interface problems and strong discontinuities in branched cracks and discontinuous grain boundary problems. It bears emphasis that the proposed enrichment functions align with those proposed in the original DE-FEM approach [10], which significantly reduced the complexity of the computer implementation when compared to GFEM/XFEM; the DE-FEM enrichment scheme therefore enables the modeling of weak discontinuity problems à la IGFEM [26] and strong discontinuity problems within a unified formulation.

Utilizing DE-FEM as the foundation of our approach capitalizes on its inherent advantages. Our method provides improvements over the methodologies employed by Daux et al. [6] and Simone et al. [7] in terms of simplicity, implementation of Dirichlet boundary conditions, and post-processing of results. Simultaneously, it enables accurate modeling of various types of intersecting discontinuities. Regarding computational cost, it is worth noting that, since discontinuities are lower-dimensional geometric manifolds—i.e., lines in 2-D and surfaces in 3-D—the additional enriched DOFs needed to capture their kinematics constitute only a small fraction of the total DOFs associated with bulk elements [40]. This difference is more pronounced as problems become asymptotically large, e.g., for higher mesh resolutions.

The numerical examples presented in Section 5 demonstrate comparable convergence properties to standard FEM when using fitted meshes. No crack tip singular enrichments are adopted in our formulation and therefore suboptimal convergence rates are attained. We recall that the error in energy norm is bounded by

$$\left\|\boldsymbol{u}-\boldsymbol{u}^h\right\|_{\mathcal{E}(\Omega)} \leq C h^{\min(p,\lambda)} \|\boldsymbol{u}\|_{\mathcal{E}(\Omega)},$$

where C is a constant, p is the polynomial order, and λ the singularity exponent. In the problems investigated herein singularities arise at crack tips in cohesive and traction-free cracks, and at junctions in the case of perfectly-bonded interfaces. For a traction-free crack $\lambda = 1/2$ and thus both FEM and DE-FEM converge suboptimally at a rate $\mathcal{O}\left(h^{1/2}\right)$. For junctions, however, there is a less severe singularity—e.g., $\lambda = 0.7256$ [36, § 5.1] for the example in § 4.2, making less stringent the need for singular enrichments. In addition, we also note that there is a large set of problems for which addressing the singularity is not as critical as in LEFM problems, e.g., in cohesive crack models where the singularity is inherently regularized by the cohesive zone. For these models the focus should be placed on accurately capturing the kinematics (displacements jumps and gradients) within the cohesive zone rather than on the singularity itself.

Despite not using singular enrichments, we note that accurate stress intensity factors are still obtained, as first shown in the original DE-FEM formulation [10]. Herein we again show that DE-FEM recovers SIFs that are as accurate as those computed in XFEM using singular enrichments by Daux et al. [6] (see results in Section 5.3.1, Section 5.3.2, and Appendix C). This is because SIFs converge with mesh size h at a rate $\mathcal{O}(h)$, which is twice as fast as the rate of convergence for the finite element solution (error in energy norm) without addressing the singularity, i.e., $\mathcal{O}\left(h^{1/2}\right)$—functionals, as the interaction integral in (18), converge at twice the rate of their argument [41]. However, our formulation does not preclude the possibility of incorporating additional singular enrichment functions to yield optimal convergence rates and even more accurate SIFs. The increased accuracy would come at the expense of a more intricate computer implementation, as large areas around singularities would need to be enriched (i.e., geometrical rather than topological enrichments). Additionally, special techniques would be required to address the loss of accuracy in blending elements and the quadrature of singular functions [32].

We achieved satisfactory results for both thermal and mechanical problems in polycrystalline materials, demonstrating effective handling of complex scenarios involving multiple junctions even with a coarse mesh. Furthermore, we showed that when dealing with displacement jumps, incorporating weak enrichments becomes essential for obtaining fully-independent kinematic fields and ensuring the proper fulfillment of the patch test. In the examination of the stress intensity factors for branched cracks, our results align with reference solutions.

While all our examples considered straight discontinuities, results presented herein can readily be extrapolated to problems where curved discontinuities are represented piece-wise linearly. It is important to note that enhancing the geometry of curved discontinuities beyond a piecewise linear representation is ineffective, as demonstrated by De Lazzari et al. [31], who combined DE-FEM with a NURBS parameterization of curved discontinuities. In that work we concluded that improving the geometry of curved discontinuities to minimize the geometry discretization error does not justify the complexities associated with the formulation and implementation. In fact, accurately modeling curved interfaces is not necessary as long as the primal field remains linear, since it is well-known that superparametric formulations induce artificial stresses even with rigid-body motions [31,42].

The methodology presented in this work therefore opens a relatively simple venue to simulate discrete crack propagation including branching and merging. Finally, although the method has been derived in a two-dimensional context, its extension to three dimensions is straightforward. The extension requires the help of a robust geometric engine, as described by Zhang et al. [29]. The only potential issue may lie in determining an efficient way of cutting elements crossed by multiple intersecting discontinuities. Yet, recent published work by Zhang et al. [35] shows that such operations can be performed robustly on complex 3-D polycrystalline microstructures discretized using structured tetrahedral meshes.

CRediT authorship contribution statement

Dongyu Liu: Writing – original draft, Visualization, Validation, Software, Methodology, Investigation, Data curation. **Jian Zhang:** Writing – review & editing. **Alejandro M. Aragón:** Writing – review & editing, Supervision, Project administration, Conceptualization. **Angelo Simone:** Writing – review & editing, Supervision, Project administration, Conceptualization.

Declaration of competing interest

The authors declare that they have no known competing financial interests or personal relationships that could have appeared to influence the work reported in this paper.

Data availability

Data will be made available on request.

Acknowledgments

Dongyu Liu gratefully acknowledges the financial support from the China Scholarship Council (CSC) under contract 201606250027.

Appendix A. Derivation of the junction enrichment

Following on the discussion of Section 3.2, and making reference to Fig. 5, the continuous component of the field at the junction can be written as

$$\widetilde{\boldsymbol{u}}_j^h = \varphi_7(\boldsymbol{x})\left(\boldsymbol{u}_7 + \gamma_7\boldsymbol{\beta}_7\right) + \varphi_8(\boldsymbol{x})\left(\boldsymbol{u}_8 + \gamma_8\boldsymbol{\beta}_8\right) + \varphi_9(\boldsymbol{x})\left(\boldsymbol{u}_9 + \gamma_9\boldsymbol{\beta}_9\right), \tag{45}$$

where we recall that $\boldsymbol{\beta}_9 = \boldsymbol{\beta}_7 + \boldsymbol{\beta}_8$. Since this function is continuous, at the junction coordinate $\boldsymbol{x}_7 = \boldsymbol{x}_8 = \boldsymbol{x}_9$ we have $\widetilde{\boldsymbol{u}}(\boldsymbol{x}_7) = \widetilde{\boldsymbol{u}}(\boldsymbol{x}_8) = \widetilde{\boldsymbol{u}}(\boldsymbol{x}_9)$. Since at this coordinate $\varphi_7(\boldsymbol{x}_7) = \varphi_8(\boldsymbol{x}_8) = \varphi_9(\boldsymbol{x}_9) = 1$, from (45) we have

$$\boldsymbol{u}_7 + \gamma_7\boldsymbol{\beta}_7 = \boldsymbol{u}_8 + \gamma_8\boldsymbol{\beta}_8 = \boldsymbol{u}_9 + \gamma_9\left(\boldsymbol{\beta}_7 + \boldsymbol{\beta}_8\right), \tag{46}$$

which can be written as

$$\begin{aligned}
&\boldsymbol{u}_7 + \gamma_7\boldsymbol{\beta}_7 = \boldsymbol{u}_8 + \gamma_8\boldsymbol{\beta}_8,\\
&\boldsymbol{u}_8 + \gamma_8\boldsymbol{\beta}_8 = \boldsymbol{u}_9 + \gamma_9\left(\boldsymbol{\beta}_7 + \boldsymbol{\beta}_8\right),\\
&\boldsymbol{u}_7 + \gamma_7\boldsymbol{\beta}_7 = \boldsymbol{u}_9 + \gamma_9\left(\boldsymbol{\beta}_7 + \boldsymbol{\beta}_8\right),
\end{aligned} \tag{47}$$

and cast into matrix form as

$$\underbrace{\begin{bmatrix} \boldsymbol{\beta}_7 & -\boldsymbol{\beta}_8 & 0\\ 0 & \boldsymbol{\beta}_8 & -\left(\boldsymbol{\beta}_7 + \boldsymbol{\beta}_8\right)\\ \boldsymbol{\beta}_7 & 0 & -\left(\boldsymbol{\beta}_7 + \boldsymbol{\beta}_8\right) \end{bmatrix}}_{\boldsymbol{A}} \begin{bmatrix} \gamma_7\\ \gamma_8\\ \gamma_9 \end{bmatrix} = \begin{bmatrix} \boldsymbol{\beta}_7\\ \boldsymbol{\beta}_8\\ \boldsymbol{\beta}_7 + \boldsymbol{\beta}_8 \end{bmatrix}, \tag{48}$$

where we employed $\boldsymbol{u}_8 - \boldsymbol{u}_7 = \boldsymbol{\beta}_7$ and $\boldsymbol{u}_9 - \boldsymbol{u}_8 = \boldsymbol{\beta}_8$. The coefficient matrix is in fact rank deficient, i.e., $\operatorname{rank}(\boldsymbol{A}) = 2$, and thus there is an infinite number of solutions. However, if one of the variables γ_i is fixed, the other two can be determined. Fixing for instance γ_7 yields

$$\gamma_8 = \frac{\boldsymbol{\beta}_7\left(\gamma_7 - 1\right)}{\boldsymbol{\beta}_8}, \quad \gamma_9 = \frac{\boldsymbol{\beta}_7}{\boldsymbol{\beta}_7 + \boldsymbol{\beta}_8}\gamma_7 - 1. \tag{49}$$

We now replace γ_8 and γ_9 in (49), and $\boldsymbol{u}_8 = \boldsymbol{u}_7 + \boldsymbol{\beta}_7$ and $\boldsymbol{u}_9 = \boldsymbol{u}_7 + \boldsymbol{\beta}_7 + \boldsymbol{\beta}_8$ in (45) to get

$$\widetilde{\boldsymbol{u}}_j^h = \left(\varphi_7(\boldsymbol{x}) + \varphi_8(\boldsymbol{x}) + \varphi_9(\boldsymbol{x})\right)\left(\boldsymbol{u}_7 + \gamma_7\boldsymbol{\beta}_7\right). \tag{50}$$

The discontinuous components at the junction, following the above derivations, can then be written as

$$\begin{aligned}
\bar{\widetilde{\boldsymbol{u}}}_j^h(\boldsymbol{x}) &= -\gamma_7\varphi_7(\boldsymbol{x})\boldsymbol{\beta}_7 - \gamma_8\varphi_8(\boldsymbol{x})\boldsymbol{\beta}_8 - \gamma_9\varphi_9(\boldsymbol{x})\boldsymbol{\beta}_9\\
&= -\gamma_7\varphi_7(\boldsymbol{x})\boldsymbol{\beta}_7 + \left(1 - \gamma_7\right)\varphi_8(\boldsymbol{x})\boldsymbol{\beta}_7 + (1 - \gamma_7)\varphi_9(\boldsymbol{x})\boldsymbol{\beta}_7 + \varphi_9(\boldsymbol{x})\boldsymbol{\beta}_8.
\end{aligned} \tag{51}$$

Appendix B. Asymptotic fields

For completeness, here we provide the asymptotic fields for the calculation of the interaction integral (18). The displacement field is given by

$$\boldsymbol{u} = \begin{bmatrix} u_x\\ u_y \end{bmatrix} = \frac{K_{\mathrm{I}}}{2E}\sqrt{\frac{r}{2\pi}}(1+\nu)\begin{bmatrix} (2\kappa - 1)\cos\frac{\theta}{2} - \cos\frac{3\theta}{2}\\ (2\kappa + 1)\sin\frac{\theta}{2} - \sin\frac{3\theta}{2} \end{bmatrix} + \frac{K_{\mathrm{II}}}{2E}\sqrt{\frac{r}{2\pi}}(1+\nu)\begin{bmatrix} (2\kappa + 3)\sin\frac{\theta}{2} + \sin\frac{3\theta}{2}\\ (3 - 2\kappa)\cos\frac{\theta}{2} - \cos\frac{3\theta}{2} \end{bmatrix}, \tag{52}$$

Table 2
Normalized SIFs for various ratios b/a and θ for the branched crack example..

b/a	θ	15°		30°		45°		60°		75°	
		DE-FEM	*	DE-FEM	*	DE-FEM	*	DE-FEM	*	DE-FEM	*
0.2	$\overline{K}_{\mathrm{I}}^{A}$	1.004	–	1.010	1.012	1.012	1.015	1.016	1.018	1.021	1.021
	$\overline{K}_{\mathrm{I}}^{B}$	0.731	–	0.681	0.667	0.535	0.528	0.333	0.335	0.122	0.122
	$\overline{K}_{\mathrm{II}}^{B}$	0.063	–	0.235	0.247	0.412	0.405	0.477	0.492	0.472	0.497
0.4	$\overline{K}_{\mathrm{I}}^{A}$	1.009	1.011	1.015	1.018	1.021	1.023	1.026	1.028	1.036	1.037
	$\overline{K}_{\mathrm{I}}^{B}$	0.753	0.729	0.672	0.659	0.506	0.504	0.295	0.295	0.064	0.066
	$\overline{K}_{\mathrm{II}}^{B}$	0.078	0.078	0.301	0.295	0.423	0.460	0.545	0.546	0.524	0.542
0.6	$\overline{K}_{\mathrm{I}}^{A}$	1.013	1.014	1.021	1.023	1.028	1.029	1.038	1.039	1.058	1.060
	$\overline{K}_{\mathrm{I}}^{B}$	0.754	0.732	0.666	0.657	0.499	0.497	0.286	0.284	0.055	0.054
	$\overline{K}_{\mathrm{II}}^{B}$	0.099	0.095	0.318	0.319	0.482	0.485	0.509	0.568	0.538	0.554
0.8	$\overline{K}_{\mathrm{I}}^{A}$	1.016	1.016	1.026	1.026	1.036	1.036	1.053	1.053	1.086	1.087
	$\overline{K}_{\mathrm{I}}^{B}$	0.748	0.735	0.667	0.658	0.495	0.495	0.283	0.281	0.058	0.056
	$\overline{K}_{\mathrm{II}}^{B}$	0.104	0.107	0.314	0.333	0.482	0.498	0.560	0.567	0.542	0.551
1.0	$\overline{K}_{\mathrm{I}}^{A}$	1.019	1.018	1.030	1.030	1.043	1.044	1.068	1.069	1.116	1.117
	$\overline{K}_{\mathrm{I}}^{B}$	0.744	0.737	0.664	0.658	0.497	0.495	0.282	0.281	0.064	0.061
	$\overline{K}_{\mathrm{II}}^{B}$	0.112	0.114	0.330	0.343	0.505	0.506	0.574	0.577	0.514	0.541
1.5	$\overline{K}_{\mathrm{I}}^{A}$	1.026	–	1.042	–	1.065	–	1.108	–	1.145	–
	$\overline{K}_{\mathrm{I}}^{B}$	0.755	–	0.666	–	0.497	–	0.284	–	0.057	–
	$\overline{K}_{\mathrm{II}}^{B}$	0.121	–	0.353	–	0.516	–	0.504	–	0.300	–
2.0	$\overline{K}_{\mathrm{I}}^{A}$	1.033	–	1.053	–	1.084	–	1.143	–	1.175	–
	$\overline{K}_{\mathrm{I}}^{B}$	0.754	–	0.669	–	0.492	–	0.289	–	0.073	–
	$\overline{K}_{\mathrm{II}}^{B}$	0.131	–	0.355	–	0.463	–	0.510	–	0.317	–

* Reference solution by Chen and Hasebe [37, Table 4].

Table 3
Normalized SIFs for various ratios a/w for the cross-shaped crack example.

a/w	0.1	0.2	0.3	0.4	0.5	0.6	0.7	0.8	0.9
DE-FEM	0.8685	0.8868	0.9117	0.9582	1.0247	1.125	1.2843	1.5958	2.2487
XFEM*	0.8653	0.8844	0.9147	0.9572	1.0253	1.1348	1.3170	1.6388	2.4395
†	0.8641	0.8800	0.9092	0.9537	1.0223	1.1300	1.2866	1.4857	–

* XFEM solution by Daux et al. [6, Table IV].
† Reference solution by Cheung et al. [38, Table 1].

and the stress field (in Voigt notation) by

$$\boldsymbol{\sigma} = \begin{bmatrix} \sigma_{xx} \\ \sigma_{yy} \\ \sigma_{xy} \end{bmatrix} = \frac{K_{\mathrm{I}}}{\sqrt{2\pi r}} \cos\frac{\theta}{2} \begin{bmatrix} 1 - \sin\frac{\theta}{2}\sin\frac{3\theta}{2} \\ 1 + \sin\frac{\theta}{2}\sin\frac{3\theta}{2} \\ \sin\frac{\theta}{2}\cos\frac{3\theta}{2} \end{bmatrix} + \frac{K_{\mathrm{II}}}{\sqrt{2\pi r}} \begin{bmatrix} -\sin\frac{\theta}{2}\left(2 + \cos\frac{\theta}{2}\cos\frac{3\theta}{2}\right) \\ \sin\frac{\theta}{2}\cos\frac{\theta}{2}\sin\frac{3\theta}{2} \\ \cos\frac{\theta}{2}\left(1 - \sin\frac{\theta}{2}\sin\frac{3\theta}{2}\right) \end{bmatrix}. \tag{53}$$

In (52) and (53) κ is Kolosov's constant, given by

$$\kappa = \begin{cases} \dfrac{3-\nu}{1+\nu} & \text{for plane stress,} \\ 3 - 4\nu & \text{for plane strain.} \end{cases} \tag{54}$$

Derivatives of the asymptotic displacement fields are obtained by the chain rule, i.e.,

$$\frac{\partial u_x}{\partial x} = \frac{\partial u_x}{\partial r}\frac{\partial r}{\partial x} + \frac{\partial u_x}{\partial \theta}\frac{\partial \theta}{\partial x} \quad \text{and} \quad \frac{\partial u_y}{\partial x} = \frac{\partial u_y}{\partial r}\frac{\partial r}{\partial x} + \frac{\partial u_y}{\partial \theta}\frac{\partial \theta}{\partial x}. \tag{55}$$

Appendix C. SIFs for branched cracks

See Tables 2–4.

Table 4
Normalized SIFs for various ratios a/w for the star-shaped crack example.

a/w	0.1	0.2	0.3	0.4	0.5	0.6	0.7	0.8	0.9
$\overline{K}_{\mathrm{I}}^{A}$	0.7588	0.7712	0.7949	0.8389	0.8941	0.9668	1.0907	1.3382	1.8737
$\overline{K}_{\mathrm{I}}^{A}$*	0.7511	0.7670	0.7931	0.8287	0.8864	0.9673	1.0971	1.3432	1.9037
$\overline{K}_{\mathrm{I}}^{A}$†	0.7408	0.7570	0.7846	0.8255	0.8815	0.9758	1.1142	–	–
$\overline{K}_{\mathrm{I}}^{B}$	0.7521	0.7694	0.8071	0.8543	0.9241	1.0455	1.2348	1.5181	1.9865
$\overline{K}_{\mathrm{I}}^{B}$*	0.7690	0.7683	0.7983	0.8466	0.9255	1.0445	1.2367	1.5624	2.1927
$\overline{K}_{\mathrm{I}}^{B}$†	0.7408	0.7578	0.7884	0.8365	0.9087	1.0182	1.1936	–	–
$\overline{K}_{\mathrm{II}}^{B}$	−0.0062	0.0001	−0.0002	0.0060	0.0158	0.0303	0.0505	0.0857	0.0533
$\overline{K}_{\mathrm{II}}^{B}$*	0.0001	0.0005	0.0021	0.0080	0.0184	0.0364	0.0593	0.0864	0.0868
$\overline{K}_{\mathrm{II}}^{B}$†	0.0000	0.0004	0.0022	0.0070	0.0168	0.0338	0.0529	–	–

* XFEM solution by Daux et al. [6, Table V].
† Reference solution by Cheung et al. [38, Table 3].

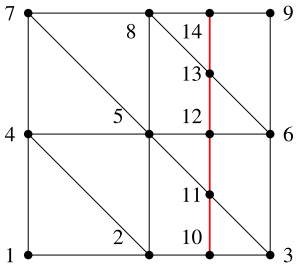

Fig. 20. Schematic diagram to illustrate the enforcement of periodic boundary conditions.

Appendix D. Periodic boundary conditions for discontinuous fields

We describe the procedure for applying periodic boundary conditions to enriched boundaries. As shown in Fig. 20, an unfitted mesh is intersected by a discontinuity segment (red line). Enrichment functions are associated with enriched nodes collocated at the intersections, i.e., $\boldsymbol{x}_i$, $i = \{10 \dots 14\}$. With reference to the displacement field, to prescribe periodicity between top and bottom edges, original mesh nodes follow standard procedures, i.e.,

$$\boldsymbol{u}_1 = \boldsymbol{u}_7, \quad \boldsymbol{u}_2 = \boldsymbol{u}_8, \quad \boldsymbol{u}_3 = \boldsymbol{u}_9. \tag{56}$$

For enriched nodes 10 and 14, it is necessary that the continuous and discontinuous components of the displacement be the same on the left sides of the discontinuity for both the top and bottom nodes, as well as on the right side for both the top and bottom nodes. For the discontinuous component, this condition is fulfilled when the displacement jumps at nodes 10 and 14

$$\begin{aligned} [\![\boldsymbol{u}\left(\boldsymbol{x}_{14}\right)]\!] &= \boldsymbol{u}\left(\boldsymbol{x}_{14}\right)|_{\Gamma^+} - \boldsymbol{u}\left(\boldsymbol{x}_{14}\right)|_{\Gamma^-} = \chi_{14}\left(\boldsymbol{x}_{14}\right)|_{\Gamma^+}\boldsymbol{\beta}_{14} - \chi_{14}\left(\boldsymbol{x}_{14}\right)|_{\Gamma^-}\boldsymbol{\beta}_{14} = [\![\chi_{14}]\!]\boldsymbol{\beta}_{14}, \\ [\![\boldsymbol{u}\left(\boldsymbol{x}_{10}\right)]\!] &= \boldsymbol{u}\left(\boldsymbol{x}_{10}\right)|_{\Gamma^+} - \boldsymbol{u}\left(\boldsymbol{x}_{10}\right)|_{\Gamma^-} = \chi_{10}\left(\boldsymbol{x}_{10}\right)|_{\Gamma^+}\boldsymbol{\beta}_{10} - \chi_{10}\left(\boldsymbol{x}_{10}\right)|_{\Gamma^-}\boldsymbol{\beta}_{10} = [\![\chi_{10}]\!]\boldsymbol{\beta}_{10}, \end{aligned} \tag{57}$$

are the same. Given that the (unit) jump of the strong enrichment functions $[\![\chi_{14}]\!]$ and $[\![\chi_{10}]\!]$ can be either positive or negative depending on how the discontinuity is defined, the constraint is expressed as

$$\operatorname{sign}\left([\![\chi_{14}]\!]\right)\boldsymbol{\beta}_{14} = \operatorname{sign}\left([\![\chi_{10}]\!]\right)\boldsymbol{\beta}_{10}. \tag{58}$$

For the continuous part, the condition $\widetilde{\boldsymbol{u}}\left(\boldsymbol{x}_{10}\right) = \widetilde{\boldsymbol{u}}\left(\boldsymbol{x}_{14}\right)$ leads to

$$\varphi_8\left(\boldsymbol{x}_{14}\right)\boldsymbol{u}_8 + \varphi_9\left(\boldsymbol{x}_{14}\right)\boldsymbol{u}_9 + \boldsymbol{\alpha}_{14} = \varphi_2\left(\boldsymbol{x}_{10}\right)\boldsymbol{u}_2 + \varphi_3\left(\boldsymbol{x}_{10}\right)\boldsymbol{u}_3 + \boldsymbol{\alpha}_{10}. \tag{59}$$

Since $\boldsymbol{u}_2 = \boldsymbol{u}_8$, $\boldsymbol{u}_3 = \boldsymbol{u}_9$ and due to the partition of unity property along the edge, $\varphi_8\left(\boldsymbol{x}_{14}\right) + \varphi_9\left(\boldsymbol{x}_{14}\right) = 1$ and $\varphi_2\left(\boldsymbol{x}_{10}\right) + \varphi_3\left(\boldsymbol{x}_{10}\right) = 1$, the above equation reduces to

$$\boldsymbol{\alpha}_{14} = \boldsymbol{\alpha}_{10}. \tag{60}$$

In summary, applying periodic boundary conditions to a discontinuous field on enriched nodes involves equating the signed strong enriched DOFs and the weak enriched DOFs.

References

[1] X.P. Xu, A. Needleman, Numerical simulations of fast crack growth in brittle solids, J. Mech. Phys. Solids 42 (9) (1994) 1397–1434, http://dx.doi.org/10.1016/0022-5096(94)90003-5.

[2] J. Zhai, M. Zhou, Finite element analysis of micromechanical failure modes in a heterogeneous ceramic material system, Int. J. Fract. 101 (1–2) (2000) 161–180, http://dx.doi.org/10.1023/A:1007545105723.

[3] P.D. Zavattieri, P.V. Raghuram, H.D. Espinosa, A computational model of ceramic microstructures subjected to multi-axial dynamic loading, J. Mech. Phys. Solids 49 (1) (2001) 27–68, http://dx.doi.org/10.1016/S0022-5096(00)00028-4.

[4] S. Weyer, A. Fröhlich, H. Riesch-Oppermann, L. Cizelj, M. Kovac, Automatic finite element meshing of planar Voronoi tessellations, Eng. Fract. Mech. 69 (8) (2002) 945–958, http://dx.doi.org/10.1016/S0013-7944(01)00124-2.

[5] A. Kuprat, D. George, G. Straub, M.C. Demirel, Modeling microstructure evolution in three dimensions with Grain3D and LaGriT, Comput. Mater. Sci. 28 (2) (2003) 199–208, http://dx.doi.org/10.1016/S0927-0256(03)00107-1.

[6] C. Daux, N. Moës, J. Dolbow, N. Sukumar, T. Belytschko, Arbitrary branched and intersecting cracks with the extended finite element method, Internat. J. Numer. Methods Engrg. 48 (12) (2000) 1741–1760, http://dx.doi.org/10.1002/1097-0207(20000830)48:12<1741::AID-NME956>3.0.CO;2-L.

[7] A. Simone, C.A. Duarte, E. Van der Giessen, A Generalized Finite Element Method for polycrystals with discontinuous grain boundaries, Internat. J. Numer. Methods Engrg. 67 (2006) 1122–1145, http://dx.doi.org/10.1002/nme.1658.

[8] A.M. Aragón, C.A. Duarte, P.H. Geubelle, Generalized finite element enrichment functions for discontinuous gradient fields, Internat. J. Numer. Methods Engrg. 82 (2) (2010) 242–268, http://dx.doi.org/10.1002/nme.2772.

[9] N. Moës, E. Béchet, M. Tourbier, Imposing Dirichlet boundary conditions in the extended finite element method, Internat. J. Numer. Methods Engrg. 67 (12) (2006) 1641–1669, http://dx.doi.org/10.1002/nme.1675.

[10] A.M. Aragón, A. Simone, The Discontinuity-Enriched Finite Element Method, Internat. J. Numer. Methods Engrg. 112 (11) (2017) 1589–1613, http://dx.doi.org/10.1002/nme.5570.

[11] Y. Toi, J.-S. Che, Computational damage mechanics models for brittle microcracking solids based on mesoscopic simulations, Eng. Fract. Mech. 48 (4) (1994) 483–498, http://dx.doi.org/10.1016/0013-7944(94)90203-8.

[12] M. Paggi, P. Wriggers, A nonlocal cohesive zone model for finite thickness interfaces – Part II: FE implementation and application to polycrystalline materials, Comput. Mater. Sci. 50 (5) (2011) 1634–1643, http://dx.doi.org/10.1016/j.commatsci.2010.12.021.

[13] H.D. Espinosa, P.D. Zavattieri, A grain level model for the study of failure initiation and evolution in polycrystalline brittle materials. Part II: Numerical examples, Mech. Mater. 35 (3) (2003) 365–394, http://dx.doi.org/10.1016/S0167-6636(02)00287-9.

[14] A.F. Bower, E. Wininger, A two-dimensional finite element method for simulating the constitutive response and microstructure of polycrystals during high temperature plastic deformation, J. Mech. Phys. Solids 52 (6) (2004) 1289–1317, http://dx.doi.org/10.1016/j.jmps.2003.11.004.

[15] J.P. Dempsey, P. Burgers, Dynamic crack branching in brittle solids, Int. J. Fract. 27 (3) (1985) 203–213, http://dx.doi.org/10.1007/BF00017968.

[16] H.P. Kirchner, Brittleness dependence of crack branching in ceramics, J. Am. Ceram. Soc. 69 (4) (1986) 339–342, http://dx.doi.org/10.1111/j.1151-2916.1986.tb04743.x.

[17] J. Åström, J. Timonen, Fragmentation by crack branching, Phys. Rev. Lett. 78 (19) (1997) 3677–3680, http://dx.doi.org/10.1103/PhysRevLett.78.3677.

[18] L. Wang, S. Hou, L. Shi, J. Solow, A numerical method for solving elasticity equations with interface involving multi-domains and triple junction points, Appl. Math. Comput. 251 (2015) 615–625, http://dx.doi.org/10.1016/j.amc.2014.11.072.

[19] Y. Chen, S. Hou, X. Zhang, A bilinear partially penalized immersed finite element method for elliptic interface problems with multi-domain and triple-junction points, Res. Appl. Math. 8 (2020) 100100, http://dx.doi.org/10.1016/j.rinam.2020.100100.

[20] T. Belytschko, H. Chen, J. Xu, G. Zi, Dynamic crack propagation based on loss of hyperbolicity and a new discontinuous enrichment, Internat. J. Numer. Methods Engrg. 58 (12) (2003) 1873–1905, http://dx.doi.org/10.1002/nme.941.

[21] T.-P. Fries, A corrected XFEM approximation without problems in blending elements, Internat. J. Numer. Methods Engrg. 75 (5) (2008) 503–532, http://dx.doi.org/10.1002/nme.2259.

[22] A. Cuba-Ramos, A.M. Aragón, S. Soghrati, P.H. Geubelle, J.-F. Molinari, A new formulation for imposing Dirichlet boundary conditions on non-matching meshes, Internat. J. Numer. Methods Engrg. 103 (6) (2015) 430–444, http://dx.doi.org/10.1002/nme.4898.

[23] I. Babuška, U. Banerjee, Stable Generalized Finite Element Method (SGFEM), Comput. Methods Appl. Mech. Engrg. 201 (2012) 91–111, http://dx.doi.org/10.1016/j.cma.2011.09.012.

[24] V. Gupta, C.A. Duarte, I. Babuška, U. Banerjee, A stable and optimally convergent generalized FEM (SGFEM) for linear elastic fracture mechanics, Comput. Methods Appl. Mech. Eng. 266 (2013) 23–39, http://dx.doi.org/10.1016/j.cma.2013.07.010.

[25] J. Haslinger, Y. Renard, A new fictitious domain approach inspired by the extended finite element method, SIAM J. Numer. Anal. 47 (2) (2009) 1474–1499, http://dx.doi.org/10.1137/070704435.

[26] S. Soghrati, A.M. Aragón, C. Armando D., P.H. Geubelle, An interface-enriched generalized FEM for problems with discontinuous gradient fields, Internat. J. Numer. Methods Engrg. 89 (8) (2012) 991–1008, http://dx.doi.org/10.1002/nme.3273.

[27] S.J. van den Boom, J. Zhang, F. van Keulen, A.M. Aragón, A stable interface-enriched formulation for immersed domains with strong enforcement of essential boundary conditions, Internat. J. Numer. Methods Engrg. 120 (10) (2019) 1163–1183, http://dx.doi.org/10.1002/nme.6139.

[28] A.M. Aragón, B. Liang, H. Ahmadian, S. Soghrati, On the stability and interpolating properties of the Hierarchical Interface-enriched Finite Element Method, Comput. Methods Appl. Mech. Engrg. 362 (2020) 112671, http://dx.doi.org/10.1016/j.cma.2019.112671.

[29] J. Zhang, S.J. van den Boom, F. van Keulen, A.M. Aragón, A stable discontinuity-enriched finite element method for 3-D problems containing weak and strong discontinuities, Comput. Methods Appl. Mech. Engrg. 355 (2019) 1097–1123, http://dx.doi.org/10.1016/j.cma.2019.05.018.

[30] D. Liu, S.J. van den Boom, A. Simone, A.M. Aragón, An interface-enriched generalized finite element formulation for locking-free coupling of non-conforming discretizations and contact, Comput. Mech. 70 (3) (2022) 477–499, http://dx.doi.org/10.1007/s00466-022-02159-w.

[31] E. De Lazzari, S.J. van den Boom, J. Zhang, F. van Keulen, A.M. Aragón, A critical view on the use of Non-Uniform Rational B-Splines to improve geometry representation in enriched finite element methods, Internat. J. Numer. Methods Engrg. 122 (5) (2021) 1195–1216, http://dx.doi.org/10.1002/nme.6532.

[32] A.M. Aragón, C.A. Duarte, Fundamentals of Enriched Finite Element Methods, First ed., Elsevier, 2023, http://dx.doi.org/10.1016/C2019-0-05419-2.

[33] C.F. Shih, R.J. Asaro, Elastic-plastic analysis of cracks on bimaterial interfaces: Part I—Small scale yielding, J. Appl. Mech. 55 (2) (1988) 299–316, http://dx.doi.org/10.1115/1.3173676.

[34] S. Soghrati, Hierarchical interface-enriched finite element method: An automated technique for mesh-independent simulations, J. Comput. Phys. 275 (2014) 41–52, http://dx.doi.org/10.1016/j.jcp.2014.06.016.

[35] J. Zhang, E. Zhebel, S.J. van den Boom, D. Liu, A.M. Aragón, An object-oriented geometric engine design for discontinuities in unfitted/immersed/enriched finite element methods, Internat. J. Numer. Methods Engrg. 123 (21) (2022) 5126–5154, http://dx.doi.org/10.1002/nme.7049.

[36] Sh. Akhondzadeh, A.R. Khoei, P. Broumand, An efficient enrichment strategy for modeling stress singularities in isotropic composite materials with X-FEM technique, Eng. Fract. Mech. 169 (2017) 201–225, http://dx.doi.org/10.1016/j.engfracmech.2016.11.019.

[37] Y.Z. Chen, N. Hasebe, New integration scheme for the branch crack problem, Eng. Fract. Mech. 52 (5) (1995) 791–801, http://dx.doi.org/10.1016/0013-7944(95)00052-W.

[38] Y.K. Cheung, C.W. Woo, Y.H. Wang, A general method for multiple crack problems in a finite plate, Comput. Mech. 10 (5) (1992) 335–343, http://dx.doi.org/10.1007/BF00364254.

[39] F. Ghahremani, Effect of grain boundary sliding on anelasticity of polycrystals, Int. J. Solids Struct. 16 (9) (1980) 825–845, http://dx.doi.org/10.1016/0020-7683(80)90052-9.

[40] S.J. van den Boom, F. van Keulen, A.M. Aragón, Fully decoupling geometry from discretization in the Bloch–Floquet finite element analysis of phononic crystals, Comput. Methods Appl. Mech. Engrg. 382 (2021) 113848, http://dx.doi.org/10.1016/j.cma.2021.113848.
[41] M.M. Chiaramonte, Y. Shen, A.J. Lew, Mapped finite element methods: High-order approximations of problems on domains with cracks and corners, Internat. J. Numer. Methods Engrg. 111 (9) (2017) 864–900, http://dx.doi.org/10.1002/nme.5486.
[42] B.A. Szabó, I. Babuška, Finite Element Analysis: Method, Verification and Validation, John Wiley and Sons, New York, 2021, http://dx.doi.org/10.1002/9781119426479.